

Revision 3, 2/2020

1 **Parageneses of TiB₂ in corundum xenoliths from Mt Carmel, Israel:**

2 **Siderophile behaviour of Boron under reducing conditions**

3
4 William L. GRIFFIN¹, Sarah E.M. GAIN^{1,2}, Martin SAUNDERS², Luca BINDI³, Olivier ALARD¹,
5 Vered TOLEDO⁴ and Suzanne Y. O'REILLY¹

6
7 ¹*ARC Centre of Excellence for Core to Crust Fluid Systems (CCFS) and GEMOC, Earth and*
8 *Planetary Sciences, Macquarie University, NSW 2109, Australia; bill.griffin@mq.edu.au*

9 ²*Centre for Microscopy, Characterisation and Analysis, The University of Western Australia,*
10 *WA 6009, Australia; martin.saunders@uwa.edu.au*

11 ³*Dipartimento di Scienze della Terra, Università di Firenze, Via La Pira 4, I-50121 Florence,*
12 *Italy*

13 ⁴*Shefa Gems, Netanya 4210602, Israel; vered@shefayamim.com*

14
15
16 **Abstract**

17
18 Titanium diboride (TiB₂) is a minor but common phase in melt pockets trapped in the
19 corundum aggregates that occur as xenoliths in Cretaceous basaltic volcanoes on Mt
20 Carmel, N. Israel. These melt pockets show extensive textural evidence of immiscibility
21 between metallic (Fe-Ti-C-Si) melts, Ca-Al-Mg-Si-O melts and Ti-(oxy)nitride melts. The
22 metallic melts commonly form spherules in the coexisting oxide glass. Most of the observed
23 TiB₂ crystallized from the Fe-Ti-C silicide melts, and a smaller proportion from the oxide
24 melts. The parageneses in the melt pockets of the xenoliths require $fO_2 \leq \Delta IW -6$, probably
25 generated through interaction between evolved silicate melts and mantle-derived CH₄+H₂
26 fluids near the crust-mantle boundary. Under these highly reducing conditions boron, like
27 carbon and nitrogen, behaved mainly as a siderophile element during the separation of
28 immiscible metallic and oxide melts. These parageneses have implications for the residence
29 of boron in the peridotitic mantle, and for the occurrence of TiB₂ in other less well-
30 constrained environments such as ophiolitic chromitites.

31

Revision 3, 2/2020

32 **Introduction**

33
34 Boron is a “quintessential element of the Earth’s upper continental crust” (Grew
35 2015). It was not created during stellar nucleosynthesis, but was introduced into Earth’s
36 mantle from the interstellar medium during planetary accretion. It has a low abundance in
37 the Solar system and hence in the bulk Earth; the estimated concentration in the Primitive
38 Upper Mantle is ca 0.26 ppm B (Palme and O’Neill 2005). Although Dobrzhinetskaya et al.
39 (2014) described boron nitride (BN; qingsongite) in a chromitite in the Luobusa ophiolite of
40 the Yarlung-Zhangbo suture zone (Tibet), reports of B-bearing phases in mantle-derived
41 rocks are extremely rare. The most well-known examples are the blue Type IIb diamonds,
42 with up to 8.4 ppm B in the famous Hope diamond (Gaillou et al., 2012). As a classic
43 incompatible element, B has been concentrated into the continental crust over time by
44 magmatic and sedimentary processes, resulting in 295 known mineral species (Grew et al.,
45 2017).

46 Titanium diboride (TiB₂) is produced on an industrial scale using a variety of high-
47 temperature techniques, including reduction of TiO₂ by reaction with boron carbide, or with
48 alkali-boron hydrides. It is valued for its extreme hardness, high melting point and high
49 thermal and electrical conductivity. It is extremely rare in nature, but was recently
50 described as inclusions in corundum separated from ophiolitic chromitites in Tibet, and
51 given the name jingsuiite (Xiong et al., 2019a,b).

52 TiB₂ also was earlier reported as inclusions in skeletal corundum aggregates found as
53 ejecta from small Cretaceous volcanoes on Mt Carmel, northern Israel (Griffin et al. 2016).
54 It is part of an unusual assemblage of minerals related to highly reducing conditions,
55 interpreted as developed in magma chambers near the crust-mantle boundary (Griffin et al.
56 2016b, 2018a, 2019a; references therein). Here the TiB₂ occurs in several distinct
57 parageneses, reflecting crystallization from both Fe-Ti silicide melts, and coexisting silicate
58 melts. The occurrence of the boride *in situ* in these aggregates provides textural evidence
59 and context that can give further insights into the behaviour of boron under highly reducing
60 conditions in the uppermost mantle.

61 62 **Occurrence**

63

Revision 3, 2/2020

64 The material described here comprises xenoliths from the pyroclastic ejecta of at least eight
65 Cretaceous (99-85 Ma) intraplate pyroclastic basaltic volcanoes exposed on Mt Carmel, in
66 northern Israel (Griffin et al. 2016b, 2018a, 2019a; references therein). Aggregates of
67 skeletal corundum crystals (Carmel Sapphire™) occur in-situ as xenoliths in the tuffs, and re-
68 deposited in nearby alluvial placers, mainly in the Kishon River. Suggestions that any of this
69 material might be of anthropogenic origin (Litasov et al. 2019a,b) have been refuted in
70 detail by Griffin et al. (2019b).

71 Melt pockets trapped within and between these rapidly-grown corundum crystals
72 can be divided into Type S (silicate melts with phenocrysts), Type A (Fe-Ti-silicides and Fe
73 alloys, representing immiscible metallic melts; Fig. 1) and Type N (dominated by Ti nitrides
74 with minor TiC) (Griffin et al. 2016b). Another paragenesis (Type DF) is represented by
75 coarser-grained xenoliths of hibonite+grossite+spinel +fluorite ± native V (Griffin et al.
76 2019a).

77

78 **Methods**

79

80 The sampling methods have been described in detail by Griffin et al. (2019a).

81 *SEM, FE-SEM, EMP*

82 Samples were mounted in epoxy blocks, polished and coated with carbon. A Zeiss
83 EVO MA15 scanning electron microscope (SEM) at the Geochemical Analysis Unit (GAU),
84 Macquarie University, Sydney, Australia was used to capture Backscattered Electron (BSE)
85 images and Energy Dispersive X-ray spectrometry (EDS) was used to map the elemental
86 composition of the samples, and to analyze phases of interest. An accelerating voltage of 15
87 keV and a beam current of 1 nA was used. Images and qualitative EDX data also were
88 collected on an FEI Teneo Field Emission Scanning Electron Microscope equipped with
89 secondary and backscattered-electron detectors and a pair of integrated Bruker Energy
90 Dispersive X-ray Spectroscopy analyzers (Bruker XFlash Series 6).

91 Major and minor elements were determined by electron microprobe (EMP) using a
92 CAMECA SX100 equipped with five wavelength-dispersive spectrometers at the Macquarie
93 University GeoAnalytical (MQGA; formerly GAU), Macquarie University, Sydney, Australia.
94 Analyses were performed using a focused beam (1-2 μm) with an accelerating voltage of 15
95 keV and a beam current of 30 nA. Calibration standards were a suite of natural and
96 synthetic minerals, including synthetic TiB₂, TiC and TiN. B, C, N and O were measured using

Revision 3, 2/2020

97 a PC2 crystal (on Spectro 4). Peak counting was 30 s, and background was counted for 15 s
98 on either side of the peak. Oxygen and carbon were corrected for blank effects (carbon
99 coating) by analysis of the synthetic Ti phases; matrix corrections were carried out by the
100 ZAF software.

101

102 *Transmission Electron Microscopy (TEM)*

103 Focused Ion Beam (FIB) foils from the region of interest were prepared for TEM using
104 two dual-beam FIB systems, an FEI Nova NanoLab 200 at UNSW and an FEI Helios G3 CX at
105 the Centre for Microscopy Characterisation and Analysis (CMCA), The University of Western
106 Australia, Perth, Australia. High Angle Annular Dark Field - Scanning Transmission Electron
107 Microscopy (HAADF-STEM) imaging and element mapping were carried out using an FEI
108 Titan G2 80-200 TEM/STEM with ChemiSTEM Technology operating at 200 kV at the Centre
109 for Microscopy Characterisation and Analysis (CMCA), The University of Western Australia,
110 Perth, Australia. The element maps were obtained by EDS using the Super-X detector on the
111 Titan with a beam size ~1 nm and a probe current of ~0.25 nA. Total acquisition times of 20-
112 30 minutes were used to obtain good signal-to-noise ratios. Electron diffraction was carried
113 out using a field limiting aperture that selected an area approximately 400nm in diameter.
114 Electron energy-loss spectroscopy (EELS) was carried out using a Gatan Enfium
115 spectrometer at the same beam size and beam current as the EDS, and at a dispersion of 0.1
116 eV/pixel.

117

118

119 *X-ray diffraction*

120 A small TiB₂ fragment was handpicked from the polished section under a reflected
121 light microscope and mounted on a 5 μm diameter carbon fiber, which was, in turn,
122 attached to a glass rod. Then, the fragment was tested by single-crystal X-ray diffraction.
123 Single-crystal X-ray studies were carried out at the Dipartimento di Scienze della Terra,
124 Università di Firenze using a Bruker D8 Venture diffractometer equipped with a Photon III
125 CCD detector, with graphite-monochromatized MoK α radiation ($\lambda = 0.71073 \text{ \AA}$), and with 70
126 s exposure time per frame; the detector-to-sample distance was 7 cm.

127 The structure was solved by direct methods in the space group *P6/mmm* and then
128 refined using the program Shelxl-97 (Sheldrick 2008). The site occupancy factor (s.o.f.) at the

Revision 3, 2/2020

129 Ti and B sites was allowed to vary (Ti and B versus structural vacancy) using scattering
130 curves for neutral atoms taken from the International Tables for Crystallography (Wilson
131 1992). Both the sites were found to be fully occupied by Ti and B, respectively and then
132 fixed in the subsequent refinement cycles. At the last refinement stage, with anisotropic
133 atomic displacement parameters, the residual value settled at $R_1(F) = 0.0517$ for 46 unique
134 reflections and 5 parameters. Crystallographic data are available as supplementary
135 material¹.

136

137 **Petrography and Parageneses**

138

139 Petrographic observations reveal two main parageneses of TiB₂ in the melt pockets
140 trapped in corundum aggregates from the Mt Carmel volcanic rocks.

141

142 *Metallic paragenesis*

143 In most occurrences, TiB₂ is closely associated with Fe-Ti silicides, TiC
144 (khamrabaevite) and TiN (osbornite; typically with O±C in solid solution), as well as the Ca-
145 Al-Mg silicate glass. The silicides typically occur as spherical bodies enclosed in corundum
146 (Fig. 1) and have sharp contacts to the silicate glasses or to phases crystallized from them
147 (Figs 2-4), consistent with an origin as metallic melts, immiscible with the Ca-Al-Mg silicate
148 melts of the Type S melt pockets. Coarser crystals of TiB₂ may contain lamellar inclusions of
149 TiN and/or TiC, as well as blobs of Fe-Ti silicides (Fig. 3a). Euhedral crystals are intergrown
150 with silicides (Fig. 3b) or surrounded by silicides and TiN (Fig. 3c). Smaller grains appear to
151 have crystallized along with TiC from spherical inclusions of Fe-Ti silicides in the corundum
152 aggregates (Fig 4); TiN commonly occurs on the rims of such silicide balls.

153 A FIB foil was prepared to examine the contact between an Fe-Ti-Cr silicide and an
154 unidentified oxide phase (nominally Mg(Al,Ti)₆(Si,Zr)O₁₂) that crystallized together with
155 carmeltazite from the associated silicate melt; the images revealed a crystal of TiB₂ that
156 clearly has grown from the silicide melt (Fig. 5). The original silicide has broken down into
157 three coexisting phases, enriched respectively in Cr, Ti and Fe (Fig. 5b; Table 2); the wavy
158 outlines between the three phases suggest that they were still molten at the time of
159 eruption. The TiB₂ crystal is zoned from a high-Cr core to a low-Cr rim (Fig. 6). The outer rim

¹ For a copy of CIF, document item, contact the Business Office of the Mineralogical Society of America.

Revision 3, 2/2020

160 contains an inclusion of a Cr,Fe-rich silicide, similar to the silicide phase in which that part of
161 the TiB₂ crystal was growing (Table 2). The negative-crystal form of this inclusion suggests
162 that it was trapped as a melt. The TiB₂ crystal also encloses scattered tiny (100 nm)
163 hexagonal (i.e. negative-crystal) inclusions of an Fe-Cr silicide, each containing a small
164 bubble (Fig. 6b). In a second FIB foil (Figure 7) the contact between a TiB₂ crystal and a TiN
165 melt is decorated with a thin film of a vanadium silicide.

166

167 *Oxide paragenesis*

168 The observations above define a paragenesis of TiB₂ + TiC + Fe-Cr-Ti silicides (melts)
169 ± TiN (melts); the illustrated microstructures indicate that these melts are immiscible with
170 the Al-Ca-Mg silicate melts of the Type S pockets. Since immiscible melts are by definition in
171 mutual equilibrium, phases in one melt should be in equilibrium with phases crystallizing
172 from the coexisting melt, and a phase that crystallizes from both melts will have the same
173 major-element composition in each melt. Therefore, in principle, TiB₂ should also be able to
174 crystallize from the silicate melts, and coexist with the early-crystallizing tistarite,
175 carmelazite and Mg-Ti-Al spinel. While rare, such parageneses have been observed. Figure
176 8 shows a large Type S melt pocket in which spinel (with oriented lamellae/needles of an
177 unidentified Ti-rich phase in the inner parts) has crystallized before tistarite. It includes an
178 irregular mass of platy TiB₂ which appears to have crystallized earlier, making it the first
179 phase to crystallize from the silicate melt. Figure 3a shows a large TiB₂ crystal in a silicate
180 melt pocket together with carmelazite and tistarite. The TiB₂ appears to have grown in the
181 silicate melt, but contains inclusions of both TiN and FeTiSi; this may represent a case in
182 which TiB₂ was simultaneously in equilibrium with the silicate melt, the TiN melt and a
183 silicide melt. In another example, the crystal of TiB₂ in Figure 9a appears to have crystallized
184 from the silicate melt together with TiC and ZrP, which also are part of the metallic
185 paragenesis. The large TiB₂ crystal and the attached ball of Fe-Ti silicide in Figure 9b appear
186 to coexist in a melt that also contains abundant blebs of Ti(N,O). Similarly, while the TiB₂ in
187 the examples shown in Figure 4 appears to have crystallized from the silicide melt, it is
188 euhedral against the silicate glass, and thus also appears to have been in equilibrium with
189 the surrounding silicate melt. Finally, Figure 10 shows an oxide assemblage in which TiB₂
190 coexists with a Ti-rich hibonite and a phase with the composition MgAl₈O₁₃, which was
191 shown by single-crystal X-ray diffraction to exhibit the spinel structure. Its probable formula

Revision 3, 2/2020

192 is $(\text{Al}_{0.56}\text{Mg}_{0.34}\square_{0.10})(\text{Al}_{1.88}\square_{0.12})\text{O}_4$, a Mg-bearing $\gamma\text{-Al}_2\text{O}_3$. This may correspond to the recently
193 described mineral deltalumite $(\text{Al}_{0.67}\square_{0.33})\text{Al}_2\text{O}_4$; Pekov et al. 2019), with Mg occupying
194 vacant sites in the spinel structure.

195

196 **Chemistry**

197 Table 1 gives electron microprobe (EMP) data on TiB_2 from a variety of parageneses;
198 Table 2 gives the compositions of phases in the images of Figures 3-11. EMP data are given
199 where available, SEM data where necessary because of small grain sizes, and
200 semiquantitative TEM-EDS in the case of the FIB foils described above. While some
201 examples of TiB_2 are essentially pure, others show solid solution of transition elements that
202 also are present in the coexisting silicide melts: Cr up to 1.9 wt %; V to 11.7 wt%; Fe to 0.9
203 wt%. These “extra” elements are unlikely to reflect overlap of the electron beam onto the
204 coexisting silicides, on three grounds. (1) V contents in TiB_2 are all higher than the V
205 contents of the coexisting silicides. (2) The partitioning of Cr and V between TiB_2 and
206 coexisting silicides is generally consistent across the available analyses, but the ratios of the
207 two elements are different in the two phases; TiB_2 contains 20-50% as much Cr as coexisting
208 silicide, and 1.2-7 times as much V. (3) The zoning of the TiB_2 shown in the FIB foil (Fig. 5c),
209 where interference is unlikely because of the thin target and small beam size, demonstrates
210 that elements such as Cr enter the TiB_2 lattice in the presence of silicide melts that carry
211 those elements. The mean of 16 EMP analyses, regardless of the variable presence of
212 transition elements, gives an average formula of TiB_2 ($\text{B}/\text{Ti} = 1.99$). Where the transition
213 elements are present, they substitute for Ti, giving a more general formula of $(\text{Ti},\text{V},\text{Cr},\text{Fe})\text{B}_2$.
214 The high level of oxygen in grain #5 (Table 1) may reflect overlap onto adjacent silicate glass;
215 however, the B/Ti of this analysis is low (1.80), which could suggest that the O is substituting
216 for B. Similarly, the C content of the TiB_2 shown in Figure 9 (Table 2) may reflect
217 interference from coexisting TiC.

218 EELS spectra for Ti in TiB_2 , TiC and TiN from these samples are similar (Fig. 12), and
219 consistent with the presence of Ti as Ti^{2+} (Stoyanov et al. 2007); this implies that boron is
220 present as B^{1-} .

221

222 **Crystallography**

Revision 3, 2/2020

223 The structure of the TiB_2 has been determined by both electron diffraction (TEM)
224 and single-crystal X-ray diffraction, on two samples with different parageneses. The
225 electron diffraction was carried out on the hexagonal plate shown in Figure 6a, representing
226 the silicide paragenesis; the diffraction pattern is shown in Figure 6b. The diffraction spots
227 form a hexagon; the planar spacing of the spots nearest the center of the pattern is *ca* 0.26
228 nm. This pattern is perfectly consistent with the [0001] zone axis of the known hexagonal
229 structure of synthetic TiB_2 (Villars and Calvert 1991).

230 The X-ray diffraction study was done using the grain illustrated in Fig. 10,
231 representing the oxide paragenesis. The structure (hexagonal, space group $P6/mmm$) is of
232 the AlB_2 -type (Villars and Calvert 1991) and consists of a simple-hexagonal lattice in which
233 HCP Ti layers alternate with graphite-like B layers. Unit cell parameters (in hexagonal
234 setting) are: $a = 3.0218(6)$ and $c = 3.2197(8)$ Å.

235

236 Discussion

237 *Relationships to Ti-nitrides*

238 The microstructural relationships among the silicides and TiB_2 on the one hand, and
239 the Ti-oxynitrides on the other, are ambiguous. The detailed chemistry and occurrences of
240 the nitrides will be discussed elsewhere. For the purposes of this report it is sufficient to say
241 that the nitrides appear to have been molten and highly mobile at the time of eruption, and
242 they commonly appear to fill skeletal cavities in the corundum, surrounding and
243 interpenetrating other phases (Figs 3a, 9b, 11) including the TiB_2 , although in other cases
244 (e.g. Fig. 3c) they appear to be in textural equilibrium with TiB_2 , or possibly exsolving from
245 silicide melts that were crystallizing TiB_2 (e.g. Fig. 4a). However, in Figure 11, the nitride
246 melt appears to post-date the TiB_2 , in which case their spatial relationship would be simply
247 coincidental, though we might still ask if the TiB_2 actually crystallized from the oxynitride
248 melt. Thus there is not at present enough evidence to define a separate $\text{TiB}_2 + \text{Ti(N, O)}$
249 paragenesis.

250

251 *Conditions of formation*

252 It is clear from the petrography that most of the observed TiB_2 crystallized from a
253 range of Fe-Ti-Cr-V silicide melts, rich in enough in carbon to precipitate abundant TiC as
254 well as the TiB_2 . The textural relationships also indicate that some of the TiB_2 crystallized

Revision 3, 2/2020

255 directly from the silicate melts now represented by the Ca-Al-Mg-Silicate glasses, while
256 those that crystallized from silicide melts were simultaneously in equilibrium with the
257 silicate melt and coexisting Ti(N,O) melts.

258 The overall picture is one of a close relationship between silicate melts, silicide
259 melts, nitrides and TiB₂. The petrography, and especially their subspherical morphology,
260 indicate that the silicide melts were immiscible with the dominant Ca-Al-Mg-Si oxide melt
261 from which corundum was crystallizing. The scarcity of boron-bearing phases in the silicate
262 melt pockets, contrasted with the relative abundance of TiB₂ associated with metallic melts,
263 suggests that B behaved as a siderophile element (B⁰) during immiscible-melt separation
264 under these reducing conditions. It partitioned strongly (though not completely) into
265 silicide melts, and then crystallized as TiB₂ either on cooling, or because immiscibility
266 concentrated B and C to an extent that forced the crystallization of borides and carbides.

267 The initial crystallization of the silicate melts formed Ti³⁺-bearing phases such as
268 tistarite and carmeltazite at estimated temperatures of 1400-1450 °C, and the implied *f*O₂ of
269 the magmatic system at this point was *ca* ΔIW-7, the approximate *f*O₂ of the 2TiO₂ → Ti₂O₃
270 + O buffer reaction (1500 °C, 1 atm; Griffin et al. 2016).

271 The buffer reaction Ti₂O₃ → 2TiO + O requires much lower *f*O₂ ≤ ΔIW -11.5 (1500 °C,
272 1 atm), whereas the lowest *f*O₂ recorded in the Mt Carmel xenolith assemblage is *ca* ΔIW -
273 10, in a hydrogen-dominated atmosphere (Griffin et al. 2019). Ti²⁺ phases normally would
274 not be stable in equilibrium with the local silicate melt (ΔIW-7 to -8). This suggests that
275 crystallisation of TiB₂ was driven by saturation in boron, in an atmosphere dominated by
276 CH₄+H₂ and with little oxygen available with which to form more conventional boron-
277 bearing phases. It may have involved a structurally-driven reaction in which Ti⁰ dissolved in
278 the silicide melt was oxidized to Ti²⁺ and B⁰ was reduced to B¹⁻. A similar mechanism would
279 apply to the crystallisation of Ti²⁺C from the same Fe-Ti-Si melts that precipitated TiB₂ (Fig.
280 1), and to the inferred separation of apparently immiscible TiN melts (Figs 2b,7).

281 In the examples shown here, TiB₂ is crystallizing at temperatures well below its
282 melting point. However, it is interesting to note that both TiB₂ and TiC have been grown
283 from molten aluminum at temperatures of 1500-1450 °C (Higashi and Atoda, 1970; Higashi
284 et al., 1976).

285

Revision 3, 2/2020

286 *Crystallization environment*

287 The earliest paragenesis in the melt pockets of these xenoliths is corundum +
288 tistarite (Ti_2O_3) + carmeltazite ($\text{ZrAl}_2\text{Ti}_4\text{O}_{11}$; Griffin et al., 2018b) + Mg-Al-Ti spinel, in a Ca-
289 Mg-Al-Si-O glass. The crystallization of these Ti^{3+} -bearing phases requires $f\text{O}_2$ at least 6 log
290 units below the Iron-Wustite buffer ($\Delta\text{IW-6}$; Griffin et al. 2016). Paragenetic studies (Griffin
291 et al. 2018a, 2019; Xiong et al. 2017) suggest that both the low $f\text{O}_2$ and the crystallization of
292 skeletal corundum reflect the interaction of differentiated mafic to syenitic magmas with
293 CH_4+H_2 at high fluid/melt ratios. The skeletal form of the corundum crystals in the
294 aggregates implies rapid crystallization from a melt supersaturated in Al_2O_3 , and probably
295 growth from a substrate. We have suggested (Xiong et al. 2017; Griffin et al. 2018a) that
296 this supersaturation was achieved by the rapid desilication of a parental melt, driven by the
297 exsolution of immiscible Fe-Ti-C-silicide melts, which also occur abundantly as inclusions in
298 the corundum (Type A pockets), and in the Type S melts. These melts crystallized
299 moissanite (SiC), TiB_2 , TiN (osbornite) and khamrabaevite (TiC); the Ti^{2+} -bearing phases and
300 the presence of native vanadium in corundum-hibonite-grossite xenoliths suggest still lower
301 $f\text{O}_2$ (Griffin et al. 2016b, 2018a, 2019a). These fluid-melt systems were sampled by eruption
302 of the host basalts, but were not directly genetically related to them; they represent much
303 shallower, pre-existing systems.

304 The P-T conditions of these melt-fluid systems are broadly constrained by
305 mineralogy, observed reactions and thermodynamic modelling. Dmisteinbergite is a
306 hexagonal to trigonal (depending on degree of Si-Al ordering) polymorph of anorthite (An;
307 Zolotarev et al. 2019). In the $\text{CaO-Al}_2\text{O}_3\text{-SiO}_2$ system, it crystallizes metastably at
308 temperatures ca 150 °C below the anorthite solidus during rapid cooling (Abe et al. 1991).
309 In the Type-S melt pockets dmisteinbergite occurs as needles and narrow laths in the $\text{Al}_2\text{O}_3\text{-}$
310 $\text{SiO}_2\text{-CaO}$ glasses. The microstructures strongly suggest a quench reaction, with
311 crystallization occurring under rapid decompression and cooling during the explosive
312 eruption of the host magma. This reflects the peritectic reaction $\text{Liq} + \text{corundum (Crn)} \rightarrow$
313 An , which is the reverse of the incongruent melting of anorthite ($\text{An} \rightarrow \text{Liq} + \text{Crn}$). This well-
314 studied reaction is constrained experimentally to pressures (P) >0.9 GPa and temperatures
315 (T) of ca 1550 °C (Goldsmith 1980). Thermodynamic modelling in the $\text{CaO-Al}_2\text{O}_3\text{-SiO}_2$ system
316 (Ottonello et al. 2013) shows that the melt-pocket glasses, which clearly were crystallizing
317 corundum (Griffin et al. 2016b, 2018a), would not be in equilibrium with corundum at $P < 1$

Revision 3, 2/2020

318 GPa, consistent with the crystallization of dmisteinbergite during decompression. However,
319 the same modelling suggests that grossite (CaAl_4O_7), which is found together with
320 corundum and hibonite ($\text{CaAl}_{11}\text{O}_{19}$) in some highly reduced xenoliths from Mt Carmel
321 (Griffin et al. 2019a) may not be stable at $P > 1$ GPa. It therefore is probable that the
322 corundum aggregates crystallized at pressures near 1 GPa.

323 Comparisons of mineral parageneses in the melt pockets with experimental studies
324 suggest that T decreased from $>1450^\circ\text{C}$ to *ca* 1200°C as $f\text{O}_2$ dropped from $\Delta\text{IW}-6$ to $\Delta\text{IW}\leq-9$
325 (Griffin et al. 2018a, 2019a; references therein). These P - T estimates (*ca* 1 GPa, 1450-1200
326 $^\circ\text{C}$) place the proposed site of fluid-melt interaction in the uppermost mantle, near the
327 crust-mantle boundary in the area, which is geophysically estimated to lie at 25-30 km
328 depth (Segev and Rybakov 2011).

329 One possible model for the crystallization environment is a magma chamber that
330 was being infiltrated from below by abundant highly reducing fluids derived from a metal-
331 saturated mantle. If this active percolation of reducing fluids results in an $f\text{O}_2$ gradient, with
332 lowest $f\text{O}_2$ at the base, this could result in the growth of a forest (or mush) of skeletal
333 corundum crystals at the bottom, where melt pockets trapped in the mush evolved under
334 progressively decreasing $f\text{O}_2$. Silicide and nitride melts typically coexist with tistarite +
335 spinel + carmeltazite + Ca-Al-Mg silicate glass, the assemblage that represents the earliest
336 stage in the crystallization sequence in these melt pockets. This seems to be consistent with
337 a relatively rapid process, in which the onset of silicide-melt immiscibility desilicated the
338 silicate melt and drove it into supersaturation in Al_2O_3 , and the rapid crystallization of the
339 corundum.

340

341 *Boron in the mantle*

342 Boron may be a “quintessential crustal element” but the boron in the crust must
343 ultimately have been derived from the mantle. Several recent studies of Type II (low-N)
344 diamonds conclude that they have formed in the sublithospheric mantle, at depths ranging
345 down to 700-800 km (Motasami et al. 2018; Korolev et al. 2018; Smith et al. 2016, 2018).
346 The CLIPPIR (Cullinan-type, large, inclusion-poor, pure, irregularly-shaped and resorbed) Ila
347 diamonds commonly carry Fe-rich metallic inclusions, which are jacketed by CH_4+H_2 fluids,
348 implying an $f\text{O}_2 \leq \text{IW}$. Smith et al. (2016) therefore argued that these large diamonds grew in
349 pools of metallic melt. The observations presented here suggest that such low- $f\text{O}_2$ metallic

Revision 3, 2/2020

350 melts would scavenge boron and carbon from surrounding mantle peridotites, only to lose
351 both to form diamond on cooling. However, given the low mean B content of the mantle
352 (<0.3 ppm), this mechanism probably would provide too little B to form blue Type IIb
353 diamonds with several ppm B. These contain oxide and silicate inclusions indicative of a
354 lower-mantle origin, but only rare metallic inclusions (Smith et al. 2018). However, in 28%
355 of the samples studied, Raman spectroscopy identified thin layers of fluid ($\text{CH}_4\pm\text{H}_2$),
356 probably formed as hydrogen escaped the inclusions and reacted with the enclosing
357 diamond, again implying an $f\text{O}_2$ of $\leq\text{IW}$, and the probable presence of metallic melts. In the
358 lower mantle, subducted crustal rocks could provide more boron, as argued by Smith et al.
359 (2018). If large Type IIb diamonds also grew in pools of metallic melt derived from crustal
360 rocks, those melts may have been able to scavenge enough boron and carbon to drive the
361 process of growing large blue diamonds.

362 TiB_2 has also been found as inclusions in corundum separated from ophiolitic
363 chromitites in Tibet (Xiong et al. 2019a,b). We have previously suggested (Griffin et al.
364 2016a; Xiong et al. 2017) that the occurrences of super-reduced assemblages with
365 corundum in ophiolitic peridotites reflect processes similar to those invoked to understand
366 the Mt Carmel assemblages. The Tibetan ophiolites also contain evidence of subduction
367 into the mantle transition zone (Griffin et al. 2016a; Zhang et al. 2017; Bindi et al. 2018;
368 references therein) prior to their rapid excavation during slab rollback. Such a scenario
369 clearly offers opportunities for the large-scale transfer of mantle-derived reduced volatiles
370 to shallow levels, accompanying partial melting of the upwelling mantle.

371 372 **Implications**

373
374 TiB_2 is widespread in the corundum aggregates that occur as xenoliths in Cretaceous
375 explosive basaltic volcanoes on Mt Carmel, N. Israel. The TiB_2 crystallized mainly from
376 metallic (Fe-Ti-C-Si) melts but also from immiscible coexisting Al-rich silicate melts. The
377 parageneses in the melt pockets of the xenoliths require $f\text{O}_2 \leq \Delta\text{IW} -6$, probably generated
378 through interaction between evolved silicate melts and mantle-derived CH_4+H_2 fluids, near
379 the crust-mantle boundary. Under these highly reducing conditions boron, like carbon and
380 nitrogen, behaved mainly as a siderophile element during the separation of immiscible
381 metallic and oxide melts.

Revision 3, 2/2020

382 These parageneses have implications for the residence of boron in the
383 sublithospheric mantle; if the oxygen fugacity of that mantle is controlled by the presence of
384 metallic Fe, the bulk of the mantle's B budget may reside in small fractions of metallic melts.
385 In that case the behaviour of boron during partial melting may depend strongly on the
386 oxygen fugacity at the point of melting, and its transfer to the crust as an incompatible
387 element might be more complex than currently assumed. The parageneses observed in the
388 corundum aggregates from Mt Carmel bear many similarities to those found in some
389 ophiolitic chromitites, and may offer a guide to the interpretation of the occurrence of TiB₂
390 in such less well-constrained environments.

391

392 **Acknowledgements**

393 We thank Tim Murphy for his assistance with the SEM and EMP analyses, and Sean Murray
394 for guidance on the FE-SEM imaging at Macquarie University. Vadim Kamenetsky is thanked
395 for providing the FE-SEM image used as Figure 3b, and its EDS analyses. We are grateful to
396 Fernando Cámara for perspicacious discussions and commentary. The MS was improved
397 through reviews by Jan Cempirek, Chi Ma and Associate Editor Ed Grew. The authors
398 acknowledge the facilities and the scientific and technical assistance of Microscopy Australia
399 at the Centre for Microscopy, Characterisation & Analysis, the University of Western
400 Australia, a facility funded by the University, State and Commonwealth Governments. The
401 study also used instrumentation at Macquarie University, funded by ARC Linkage
402 Infrastructure, Equipment and Facilities (LIEF) and Department of Education and Training
403 (DEST) Systemic Infrastructure Grants. Luca Bindi thanks MIUR-PRIN2017, project "TEOREM
404 deciphering geological processes using Terrestrial and Extraterrestrial ORE Minerals", prot.
405 2017AK8C32. This is contribution 1427 from the ARC Centre of Excellence for Core to Crust
406 Fluid Systems (<http://www.ccfs.mq.edu.au>), and contribution 1368 from the GEMOC ARC
407 National Key Centre (<http://www.gemoc.mq.edu.au>).

408 **References**

409 Abe, T., Tsukamoto, K., Sunagawa, I (1991) Nucleation, growth and stability of CaAl₂Si₂O₈
410 polymorphs. *Phys. Chem. Minerals*, 17, 473-484.
411 Bindi, L., Griffin, W.L., Panero, W., Sirotkina, E., Bobrov, A., and Irifune, T. (2018) High-
412 pressure synthesis of inverse ringwoodite sheds light on the subduction history of
413 Tibetan ophiolites. *Scientific Reports*, 8, 5457.

Revision 3, 2/2020

- 414 Dobrzhinetskaya, L.F., Wirth, R., Yang, J., Green, H.W., Hutcheon, I.D., Weber, P.K., and Grew,
415 E.S. (2014) Qingsongite, natural cubic boron nitride: The first boron mineral from the
416 Earth's mantle. *American Mineralogist*, 99, 764-772.
- 417 Goldsmith, J.R. (1980) The melting and breakdown reactions of anorthite at high pressures
418 and temperatures. *American Mineralogist*, 65(3-4), 272-284.
- 419 Gaillou, E., Post, J.E., Rost, D., and Butler, J.E. (2012) Boron in natural type IIb blue
420 diamonds: chemical and spectroscopic measurements. *American Mineralogist*, 97,
421 1-18.
- 422 Grew, E.S. (2015) Boron – the crustal element. *Elements*, 13, 162-163.
- 423 Grew, E.S., Hystad, G., Hazen, R.M., Golden, J., Krivovichev, S.V. and Gorelova, L.A. (2017)
424 How many boron minerals occur in Earth's upper crust? Invited Centennial Paper,
425 *American Mineralogist*, 102, 1573-1587.
- 426 Griffin, W.L., Afonso, J.C., Belousova, E.A., Gain, S.E., Gong, X-H., González-Jiménez, J.M.,
427 Howell, D., Huang, J-X., McGowan, N., Pearson, N.J., Satsukawa, T., Shi, R., Williams,
428 P., Xiong, Q., Yang, J-S., Zhang, M., and O'Reilly, S.Y. (2016a) Mantle Recycling:
429 Transition-Zone metamorphism of Tibetan ophiolitic peridotites and its tectonic
430 implications. *Journal of Petrology*, 57, 655-684.
- 431 Griffin, W.L., Gain, S.E.M., Adams, D.T., Huang, J-X., Saunders, M., Toledo, V., Pearson, N.J.,
432 and O'Reilly, S.Y. (2016b) First terrestrial occurrence of tistarite (Ti₂O₃): Ultra-low
433 oxygen fugacity in the upper mantle beneath Mt Carmel, Israel. *Geology*, 44, 815-
434 818.
- 435 Griffin, W.L., Huang, J-X., Thomassot, E., Gain, S.E.M., Toledo, V., and O'Reilly, S.Y., (2018a)
436 Super-reducing conditions in ancient and modern volcanic systems: Sources and
437 behaviour of carbon-rich fluids in the lithospheric mantle. *Mineralogy and*
438 *Petrology*, 112, Supp. 1, 101-114.
- 439 Griffin, W.L., Gain, S.E.M., Bindi, L., Toledo, V., Cámara, F., Saunders, M., and O'Reilly, S.Y.
440 (2018b) Carmeltazite, ZrAl₂Ti₄O₁₁, a new mineral trapped in corundum from volcanic
441 rocks of Mt Carmel, northern Israel. *Minerals*, 8, 601-612.
- 442 Griffin, W.L., Gain, S.E.M., Huang, J-X., Saunders, M., Shaw, J., Toledo, V., and O'Reilly, S.Y.
443 (2019a) A terrestrial magmatic hibonite-grossite-vanadium assemblage: desilication
444 and extreme reduction in a volcanic plumbing system, Mt Carmel, Israel. *American*
445 *Mineralogist*, 104, 207-219.
- 446 Griffin, W.L., Toledo, V., and O'Reilly, S.Y. (2019b) Discussion of "Enigmatic super-reduced
447 phases in corundum from natural rocks: Possible contamination from artificial
448 abrasive materials or metallurgical slags" by Litasov et al. (2019). *Lithos* 348-349,
449 105122
- 450 Higashi, I., and Atoda, T. (1970) Growth of titanium diboride single crystals in molten
451 aluminum. *Journal of Crystal Growth*, 7, 251-253.
- 452 Higashi, I., Takahashi, Y. and Atoda, T. (1976) Crystal growth of borides and carbides of
453 transition metals from molten aluminium solutions. *Journal of Crystal Growth*, 33,
454 207-211.
- 455 Korolev, N., Kopylova, M., Gurney, J.J., Moore, A.E., and Davidson, J. (2018) The origin of
456 Type II diamonds as inferred from Cullinan mineral inclusions. *Mineralogy and*
457 *Petrology*, 112, Suppl. 1, S275-S289.

Revision 3, 2/2020

- 458 Litasov, K.D., Kagi, H., Bekker, T.B. (2019a) Enigmatic super-reduced phases in corundum
459 from natural rocks: Possible contamination from artificial abrasive materials or
460 metallurgical slags. *Lithos* 340-341, 181-190.
- 461 Litasov, K.D., Bekker, T.B., Kagi, H., (2019b) Reply to the discussion of "Enigmatic super-
462 reduced phases in corundum from natural rocks: Possible contamination from
463 artificial abrasive materials or metallurgical slags" by Litasov et al. (*Lithos*, v.340-341,
464 p.181-190) by W.L. Griffin, V. Toledo and S.Y. O'Reilly.
465 *Lithos*, <https://doi.org/10.1016/j.lithos.2019.105170>
- 466 Ottonello, G., Attene, M., Ameglio, D., Belmonte, D., Zuccolini, M.V., and Natali, M. (2013)
467 Thermodynamic investigation of the CaO–Al₂O₃–SiO₂ system at high P and T
468 through polymer chemistry and convex-hull techniques. *Chemical Geology*, 346, 81-
469 92.
- 470 Palme, H., and O'Neill, H. St C. (2005) Cosmochemical estimates of mantle composition. In:
471 Carlson, R.W. (ed) *Treatise on Geochemistry. Volume 2: The Mantle and Core*.
472 Elsevier-Pergamon, Oxford, p 1-38.
- 473 Pekov, I.V., Anikin, L.P., Chukanov, N.V., Belakovskiy, D.I., Yapaskurt, V.O., Sidorov, E.G.,
474 Britvin, S.N., and Zubkova, N.V. (2019) Deltalumite, a new natural modification of
475 alumina with spinel-type structure. *Zapiski RMO*, 148, 45-58.
- 476 Segev, A., and Rybakov, M., (2011) History of faulting and magmatism in the Galilee (Israel)
477 and across the Levant continental margin inferred from potential field data. *Journal*
478 *of Geodynamics*, 51, 264-284.
- 479 Sheldrick, G.M. (2008) A short history of SHELX. *Acta Crystallographica*, A64, 112–122.
- 480 Smith, E.M., Shirey, S.B., Nestola, F., Bullock, E.S., Wang, J., Richardson, S.H., and Wang, W.
481 (2016) Large gem diamonds from metallic liquid in earth's deep interior. *Science*,
482 354, 1403-1405.
- 483 Smith, E.M., Shirey, S.B., Richardson, S.H., Nestola, F., Bullock, E.S., Wang, J., and Wang, W.
484 (2018) Blue boron-bearing diamonds from Earth's lower mantle. *Nature*, 560, 84-
485 87.
- 486 Stoyanov, E., Langenhorst, F., and Steinle-Neumann, G. (2007) The effect of valence state
487 and site geometry on Ti *L*_{3,2} and O *K* electron energy-loss spectra of Ti_xO_y phases.
488 *American Mineralogist*, 92, 577-586.
- 489 Villars, P., and Calvert, L.D. (1991) *Person's Handbook of Crystallographic Data for*
490 *Intermetallic Phases* (American Society for Metals, Materials Park, OH 44073, 1991 &
491 1997), second Edition, 1991, and Desk Edition, 1997.
- 492 Wilson, A.J.C. Ed. (1992) *International Tables for Crystallography, Volume C: Mathematical,*
493 *physical and chemical tables*. Kluwer Academic, Dordrecht, NL.
- 494 Xiong, Q., Griffin, W.L., Huang, J-X., Gain, S.E.M., Toledo, V., Pearson, N.J., and O'Reilly, S.Y.
495 (2017) Super-reduced mineral assemblages in "ophiolitic" chromitites and peridotites:
496 The view from Mt Carmel. *European Journal of Mineralogy*, 29, 557-570.
- 497 Xiong, F., Xu, X., Mugnaioli, E., Gemmi, M., Wirth, R., Grew, E.S. and Robinson, P.T. (2019a)
498 Potential new titanium minerals in corundum from the Cr-11 chromitite orebody,
499 Luobusa ophiolite, Tibet, China: Evidence for super-reduced mantle derived fluids?
500 *Geological Society of America Abstracts with Programs*. Vol. 51, No. 5 doi:
501 [10.1130/abs/2019AM-333493](https://doi.org/10.1130/abs/2019AM-333493).
- 502 Xiong, F., Xu, X., Mugnaioli, E., Gemmi, M., Wirth, R., Grew, E.S. and Robinson, P.T. (2019b)
503 Jingsuiite, IMA 2018-117b. *CNMNC Newsletter No. 52; Mineralogical Magazine*, 83,
504 <https://doi.org/10.1180/mgm.2019.73>

Revision 3, 2/2020

- 505 Yan, H-Y., Wei, Q., Chang, S-M., and Guo, P. (2011) A first-principle calculation of structural,
506 mechanical and electronic properties of titanium borides. *Trans. Nonferrous Met.*
507 *Soc. China*, 21, 1627-1633.
- 508 Zhang, Y., Jin, Z., Griffin, W.L., Wang, C., and Wu, Y. (2017) High-pressure experiments
509 provide insights into the Mantle Transition Zone history of chromitite in Tibetan
510 ophiolites. *Earth and Planetary Science Letters*, 463, 151-158.
- 511 Zolotarev, A.V., Krivovichev, S.V., Panikorovskii, T.L., Gurzhiy, V.V., Bocharov, V.N, and
512 Rassomokhin, M.A. (2019). Dmisteinbergite, $\text{CaAl}_2\text{Si}_2\text{O}_8$, a metastable polymorph of
513 anorthite: Crystal-structure and Raman spectroscopic study of the holotype
514 specimen. *Minerals* 9, 570-582.

515
516
517

518 **Figure captions**

519

520 Figure 1. BSE images of typical Fe-Ti silicide balls, enclosed in melt pockets within corundum
521 aggregates in the ejecta of Cretaceous volcanoes on Mt Carmel, N. Israel. In each case the
522 original metallic melts have unmixed into mutually immiscible Ti-rich (dark) and Ti-poor
523 (light) members prior to or during eruption.

524

525 Figure 2. Multi-element phase map showing immiscibility between Fe-Ti silicide melt and
526 silicate melt, which has partially crystallized as a complex Mg-Al-Ti-Zr silicate and
527 carmeltazite. Small grains of TiB_2 are scattered within the FeTiSi phase. Black areas
528 represent vesicles; orange phase is Ti(N,O) .

529

530 Figure 3. BSE images of TiB_2 associated with Fe-Ti-silicide melts. a, crystal of TiB_2 with
531 inclusions of TiN and FeTiSi . Associated phases, crystallized from the silicate melt, are
532 tistarite and carmeltazite. b, euhedral crystal of TiB_2 is rimmed by $\text{TiFe}_2(\text{Si,P})$ and Ti(N,O) ,
533 separated from the host corundum by a high-K glass. c, euhedral crystal of TiB_2 enclosed in a
534 complex silicide $(\text{Fe,Mn,Ti,Cr})_3\text{Si}$, which is surrounded by a large blob of Ti(N,O) that is also
535 in contact with a ball of $(\text{Fe,Ti})_2\text{Si}$. The wavy contacts between the silicides and the nitride,
536 and between the nitride and the silicate melt or the host corundum, suggest that the
537 silicides and the nitride were trapped as melts between growing corundum crystals. The
538 bright phases at top are $(\text{Zr,Ti})_2\text{O}_3$, in a silicate glass

539

540 Figure 4. BSE images of TiB_2 on the rims of silicide balls. a, FeTiSi ball (unmixing into at least
541 3 mutually immiscible components) has crystals of TiB_2 and blobs of Ti(N,O) on the rim. b,
542 FeTiSi ball with crystals of TiB_2 embedded in rim. c, ball of $(\text{Fe,Cr,V})_2\text{Si}$ with V-bearing TiB_2
543 on the rim, surrounded by silicate glass. d, closeup of top of image (c), illustrating the euhedral
544 nature of TiB_2 crystals toward both glass and silicide.

545

546 Figure 5. STEM-EDS and HAADF maps of FIB foil showing a euhedral TiB_2 crystal in Fe-Ti-Cr
547 silicide in contact with an unidentified oxide phase. a, amorphous Ca-rich phase and TiS
548 associated with a vein of amorphous carbon along the contact. b, element maps illustrating
549 unmixing of the silicide into Ti-rich, Fe-Cr-rich and Fe-rich components (Table 2).

550

Revision 3, 2/2020

551 Figure 6. Details of the foil shown in Figure 5. a, HAADF and STEM-EDS maps showing
552 zoning of TiB_2 crystal from Cr-rich core to Ti-rich rim. Note small inclusion of Cr-rich silicide
553 in rim of TiB_2 , indicating that unmixing of the silicide melt occurred before or coevally with
554 growth of the TiB_2 rim; also note a train of minute inclusions cutting across the top of the
555 crystal. b, electron-diffraction pattern from the TiB_2 crystal and closeup of one of the small
556 inclusions, consisting of a hexagon of Fe-Cr-rich silicide and a void.

557
558 Figure 7. FIB-TEM image and element maps of contact between TiB_2 and $Ti(N,O)$, showing a
559 thin vein of a vanadium silicide along the contact.

560
561 Figure 8. BSE images of TiB_2 included in spinel. a, Type S melt pocket with large spinel grain
562 with oriented Ti-rich needles in core, and large inclusion of TiB_2 . Spinel rim overgrows
563 abundant tistarite. Quench crystals of dmisteinbergite (a polymorph of anorthite) in a
564 matrix of silicate glass reflect the Ca-Al rich nature of the silicate melt. b, closeup showing
565 lamellar crystal of TiB_2 in spinel with unidentified Ti-rich needles. Light bands in the TiB_2 are
566 a Ti-nitride phase.

567
568 Figure 9. BSE images of TiB_2 parageneses. a, TiB_2 crystal in silicate glass, accompanied by
569 TiC , Ti_2Si and ZrP . b, a compound grain of TiB_2 and a silicide alloy that has unmixed into Fe-
570 rich and Ti-rich components. The silicate glass in the right-hand end of the melt inclusion is
571 full of amoeboid blobs of $Ti(N,O)$.

572
573 Figure 10. BSE image of a melt inclusion in corundum, containing a crystal of TiB_2
574 embedded in a Mg,Ti-rich variety of hibonite, and a crystal of the phase $MgAl_8O_{13}$, a possible
575 analog to deltalumite. Small bright blebs in a central vein are ZrP .

576
577 Figure 11. BSE image of an irregular crystal of TiB_2 (dark grey) inside a skeletal crystal of
578 corundum (black); the skeletal cavities are filled by a mixture of $Ti(N,O)$ (white) and silicate
579 glass (pale grey). The nitride phase appears to intrude the TiB_2 grain.

580
581 Figure 12. EELS spectra of Ti in TiB_2 , TiC and TiN .

582

Table 1. Electron microprobe analyses (wt% of elements) and atomic proportions of TiB₂

Sample	1124C	1124E	1124E	1124E	NGC #12	1124E	mean
	<i>n</i> =1	<i>n</i> =4	<i>n</i> =1	<i>n</i> =1	<i>n</i> =6	<i>n</i> =3	
Ti	67.49	63.22	58.87	60.58	66.56	67.58	65.12
Cr	0.02	0.93	1.89	0.93	0.25	0.21	0.54
Al	0.57	0.00	0.00	0.02	0.02	0.03	0.05
V	0.10	3.92	11.00	6.97	1.00	1.03	2.68
B	27.50	30.58	30.38	32.0	30.98	31.24	30.74
Si	0.02	0.00	0.00	0.15	0.01	0.00	0.02
Mn	0.00	0.45	0.00	0.03	0.00	0.00	0.12
Fe	0.00	0.90	0.00	0.74	0.01	0.00	0.28
C	0.00	0.00	0.00	0.00	0.00	0.00	0.01
N	0.00	0.00	0.00	0.00	0.00	0.00	0.01
O	3.70	0.00	0.00	0.00	0.00	0.00	0.24
Total	99.40	100.00	102.14	101.42	98.84	100.27	99.80
at %							
Ti	33.50	30.63	28.65	28.80	35.13	32.89	31.60
Cr	0.01	0.42	0.85	0.41	0.12	0.05	0.24
Al	0.50	0.00	0.00	0.00	0.02	0.04	0.04
V	0.05	1.82	5.03	3.11	0.50	0.47	1.23
B	60.43	66.57	65.47	67.36	64.26	66.55	66.50
Si	0.02	0.00	0.00	0.13	0.01	0.04	0.05
Mn	0.00	0.19	0.00	0.01	0.00	0.00	0.05
Fe	0.00	0.38	0.00	0.31	0.01	0.00	0.11
C	0.00	0.00	0.00	0.00	0.00	0.00	0.00
N	0.00	0.00	0.00	0.00	0.00	0.00	0.00
O	5.49	0.00	0.00	0.00	0.00	0.00	0.91
Total	100.00	100.00	100.00	100.10	100.10	100.00	99.80
B/(Ti+Al+Cr+V)	1.77	2.03	1.90	2.08	1.80	1.99	2.01
description	isolated inclusion	boride xl in ball	boride xl in ball	boride xl in ball	incl. in Type S pocket	lamellar incl. in spinel	

Typical 1s precision is 1-2 % for major elements, and 5-10% for minor elements.

Table 2. EDS and EMP analyses of phases associated with selected occurrences of TiB₂

Analyses are EDS unless indicated as EMP

Figure Mount no. Sample no.	Fig. 2 Mount 1 49-50/9					Fig. 3a WLG1124E 1124E/12					Fig. 3b NGC-55 1124				Fig. 3c Corundum- 479G-03
	TiB ₂ n=3	MgTi ₂ Al ₄ (Si,Zr) ₂ O ₁₂ EMP n=2	silicide 1 (Fe,Ti,Al) ₂ Si	silicide 2 FeTiSi	TiS n=3	TiB ₂ n=3	TiB ₂ EMP n=1	Ti(N,O,C) EMP n=3	silicide 1 (Fe,Mn,Cr) ₃ Si	silicide 2 FeTiSi	TiB ₂ n=2	silicide 1 FeTi(Si,P)	silicide 2 (Ti,Fe,Cr) ₃ Si	Ti(N,O)	TiB ₂
wt%															
Si	1.21	5.00	23.9	20.7				13.4	18.4						
Zr		4.32				0.25									
Ti	56.5	20.77	40.7	31.7	54.6	71.1	61.58	75.01	5.3	29.3	71.1	30.2	56.6	77.0	
Al		21.29	8.3	4.0			0.02				0.1				
Cr	2.1		3.2	2.3		2.0	0.92	4.5	3.0			3.9	1.3		
V	4.1					2.1	6.97	0.41	0.84			1.6	0.8		
P			0.09	0.27					0.58			4.7	0.4		
W									0.93						
Fe	1.31	0.02	22.6	40.0		0.33	0.74	66.4	41.1			41.0	22.7		
Ni															
Mn		0.03	1.2	1.1	0.7			7.8	4.2			0.7	0.4		
Mg		5.28													
Ca		0.01													
Ba															
Na															
K															
S					38.9										
F															
B	34.3					23.9	29.51				30.8			30.9	
N								14.9					18.1		
C								2.5							
O		40.49			4.0			8.57					8.5		
sum	99.5	97.2	100.0	100.1	98.2	99.7	99.9	101.0	97.8	98.6	102	96.9	96.9	103.6	
other phases*											Ti*,CTAZ				
Dcr Tib/silic	0.66					0.44	0.31							0	
DV Tib/silic	>4					5.12	8.30							0	
atomic %															
Si	0.95	4.24	34.04	31.7				23.70	30.08			24.36	24.08		
Zr		1.13				0.08									
Ti	26.0	10.32	34.01	28.34	48.4	39.3	30.75	46.32	5.50	28.11	29.7	29.17	54.41	46.9	
Al		18.78	12.31	6.34											
Cr	0.89		2.46	1.89		1.02	0.42	4.30	2.65			3.49	1.15		
V	1.77					1.09	3.27	0.40	0.76			1.46	0.72		
P			0.12	0.37					0.86			7.02	0.59		
W									0.23						
Fe	0.52	0.01	16.19	30.65		0.16	0.32	59.05	33.8			33.94	18.7		
Ni															
Mn		0.01	0.87	0.86				7.05	3.51			0.59	0.34		
Mg		5.18													
Ca															
Ba															
Na															
K															
S					51.6										
F															
B	69.9					58.4	65.24				70.3			66.1	
N								31.45					37.7		
C								6.15							
O		60.23						15.83					15.5		
sum	100.03	99.90	100.00	100.15	100.00	100.1	100.0	99.8	100.0	100.0	100.00	100.03	99.99	100.1	

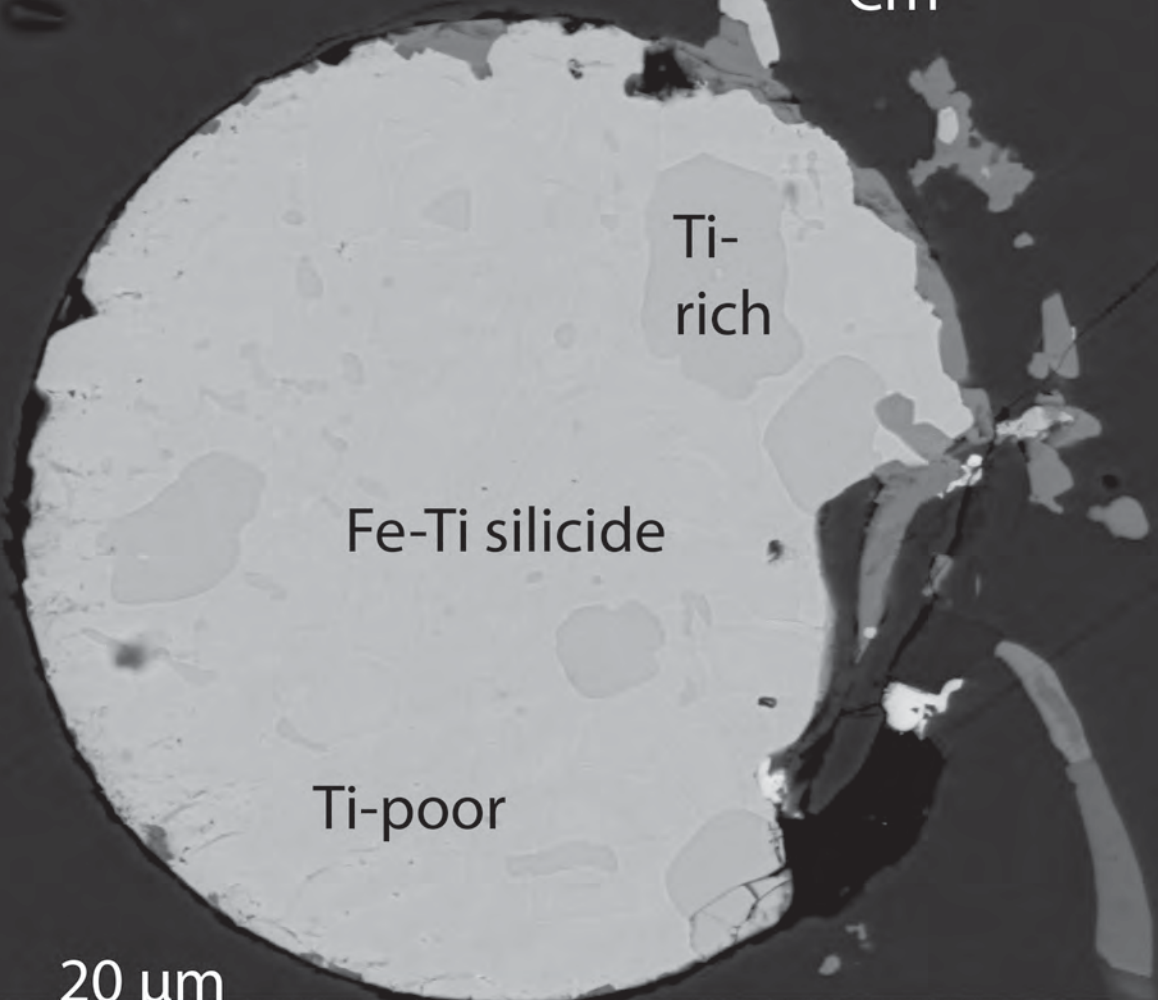
* T*, tistarite; CTAZ, carmelztazite

-SY	Fig. 4a WLG1124B 1124B/7				Fig. 4b Mount 1 49-50/11				Fig. 4c,d WLG1124B 1124B/7						Fig. 5 Mount 1 49-50/9			TEM-EDS	
	TiB ₂ EMP n=2	Ti(N,O) EMP n=2	silicide 1 (Ti,Fe) ₂ (Si,P)	silicide 2 Ti ₃ (Si,P)	TiB ₂	silicide FeTiSi	Ti oxide 1 Ti ₄ AlO ₅	Ti oxide 2 Ti ₅ Al ₂ O ₈	TiB ₂	silicide Fe ₃ Si	TiB ₂ n=4	Ti(N,O,C) EMP n=3	silicide (Fe,Cr,Ti) ₂ Si	silicate	sulfide TiS	TiB ₂ core	TiB ₂ rim	sulfide TiS	
			15.2	14.6		20.1			2.1	13.4	1.7	0.24	20.5	9.8 7.3					
69.42 0.06	79.8	64.5	84.4	70.1	35.9	66.3 8.7	54.9 13.2	27	0.3	55.3 0.75	75.2 0.06	7.2 0.92	17.8 20.4	49.7	31.2	31.1	53.8		
0.22		2.3 1.5 9.4		0.7 2.2	2.3 1.2 0.41			4.0 13.5 4.1	5.1 1.8	2.8 12.5		12.8 5.0 0.61			2.1 3.5	0.12			
		6.6 0.61	0.78	0.30	36.6 0.81			13.4	79.0	4.3	0.05	51.7 1.4		0.53 0.74	0.46	0.26		0.2	
																		45.2	
29.87				26.1				35.5		22.5								37.4	32.8
	9.5										10.7 4.0 8.5			11.0					
99.6	99.7	100.1	99.8	99.4	97.3	24.9 99.9	31.8 99.9	99.6	99.6	99.8	99.2	100.1	99.7	95.3	74.7	64.3	99.2		
				Ti* 0.30 1.8				CTAZ 0.78 7.5		0.22 2.50					0.51 1.40				
		19.11	22.5		32.28			1.61	23.6	1.64		32.72	8.39 1.93						
34.4 0.05	55.7	58.79	76.33	37.6	33.83	42.44 9.88	31.65 13.5	12.16		31.2 0.75	48.9 0.07	6.74 1.53	8.95 18.19	49.45	15.3 0.4	18.4	44.4		
0.1		1.93 1.28 13.24	1.09	0.34 1.1	2 1.06 0.6			1.66 5.72 2.85	4.8 1.7	1.45 6.6	0.3	11.03 4.4 0.94			0.95 1.65	0.07			
		5.16 0.48		0.14	29.56 0.67			5.17	69.9	2.08		41.5 1.14		0.64 0.45	0.19	0.13			
																		55.6	
65.48				61.3				70.8		56.23					81.5	81.5			
	22.6										23.79 10.37 16.55		54.43						
100.00	100.04	99.99	99.92	100.48	100.00	100.00	100.00	99.97	100.00	100.00	100.00	100.00	100.01	100.00	100.0	100.1	100.0		

				Fig. 8 WLG1124B 1124B/15					Fig. 9a SY-01 1129			Fig. 10 SY-01 1129		Fig. 11 WLG1124E 1124E/8		
silicide 9 (Ti,Fe) ₃ Si ₂	silicide 7 (Fe,Ti,Cr)Si	silicide 6 FeTiSi	incl in TiB ₂ FeTiSi	TiB ₂	TiB ₂ EMP n=4	spinel	Ti(N ₂ O ₂ C) EMP n=4	glass	TiB ₂	ZrP	glass	MgAl ₆ O ₁₃	hibonite	TiB ₂ EMP n=4	Ti ₂ (N ₂ O) ₃ EMP n=3	
27.3	33.3	23.0	23.5		0.05			21.6		0.32 69.4	19.6	0.12		0.01 0.04	0.31	
37.0	17.5	27.6	28.2	71.0	68.35 0.05 0.12 1.03	3.9 37.8	74.55 0.09	0.51 20.8	69.1	4.5 0.2	0.3 24.8	55.1	53.3	66.6 0.02 0.25 1.0	67.24 0.13 0.02 0	
9.1	15.5	4.1	4.1				0.08									
3.7	3.3	2.5	2.5													
21.1	27.8	40.6	39.3											0.01	0	
1.2	2.1	1.6	1.5			11.4		14.65				0.84 17.4 1.5 0.88 3.1 0.37 0.39	6.4	0.12 0.45 5.96	0.00 0	
				29.0	31.2		14.50 2.00		27.6						0	
						39.5 92.6	9.00 100.2	38.5 96.5	3.0		30.3	38.4	38.0	n/a n/a	22 n/a	
99.4	99.5	99.4	99.1	100.0	100.84				99.7	98.7	99.5	100.0	97.8	98.9	99.2	
				Ti ⁴⁺ , CTAZ												
40.6	48.4	36.5	36.6		0.04			17.73		0.68 45.86	16.84	0.1		0.01 0.01	0.31	
32.3	14.9	25.1	25.8	35.6	32.9 0.04 0.05 0.47	1.84 31.69	46.82 0.1	0.25 17.77	34.00	5.69 0.44	0.16 22.02	43.3	43.7	32.48 0.02 0.14 0.5	39.18 0.13	
7.3	12.2	3.4	3.5				0.05									
3.0	2.6	2.1	2.2						46.99							
15.8	20.3	31.7	30.8			10.61		8.43								
0.9	1.6	1.2	1.2									5.56	0.05 0.41 3.29			
				64.4	66.5		31.12 5.01		60.12					66.93 n/a	43.61	
100.0	100.0	100.0	100.0	100.0	100.0	100.0	100.0	100.0	100.0	99.7	99.7	100.0	100.0	n/a 100.1	16.56 99.8	

BSE

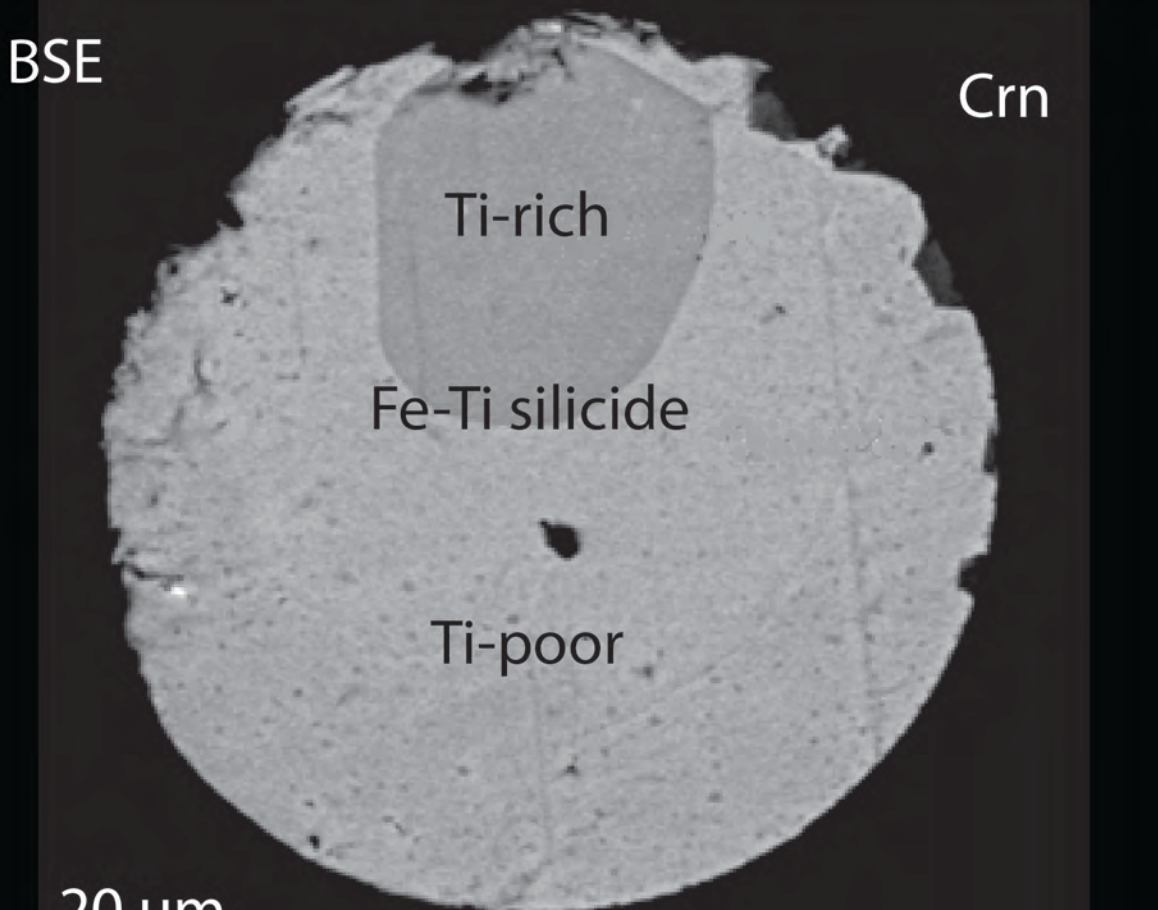
Crn



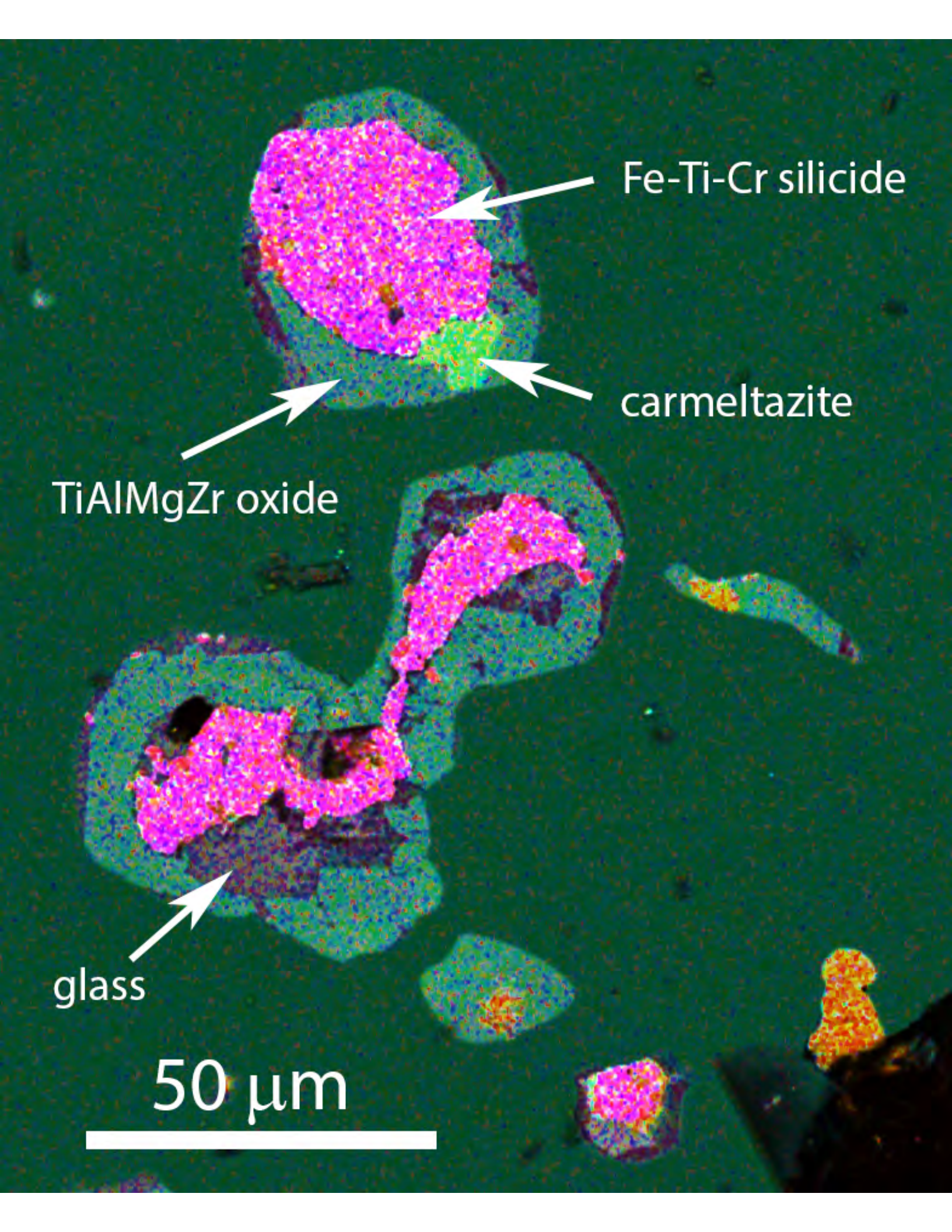
20 μm

BSE

Crn



20 μm



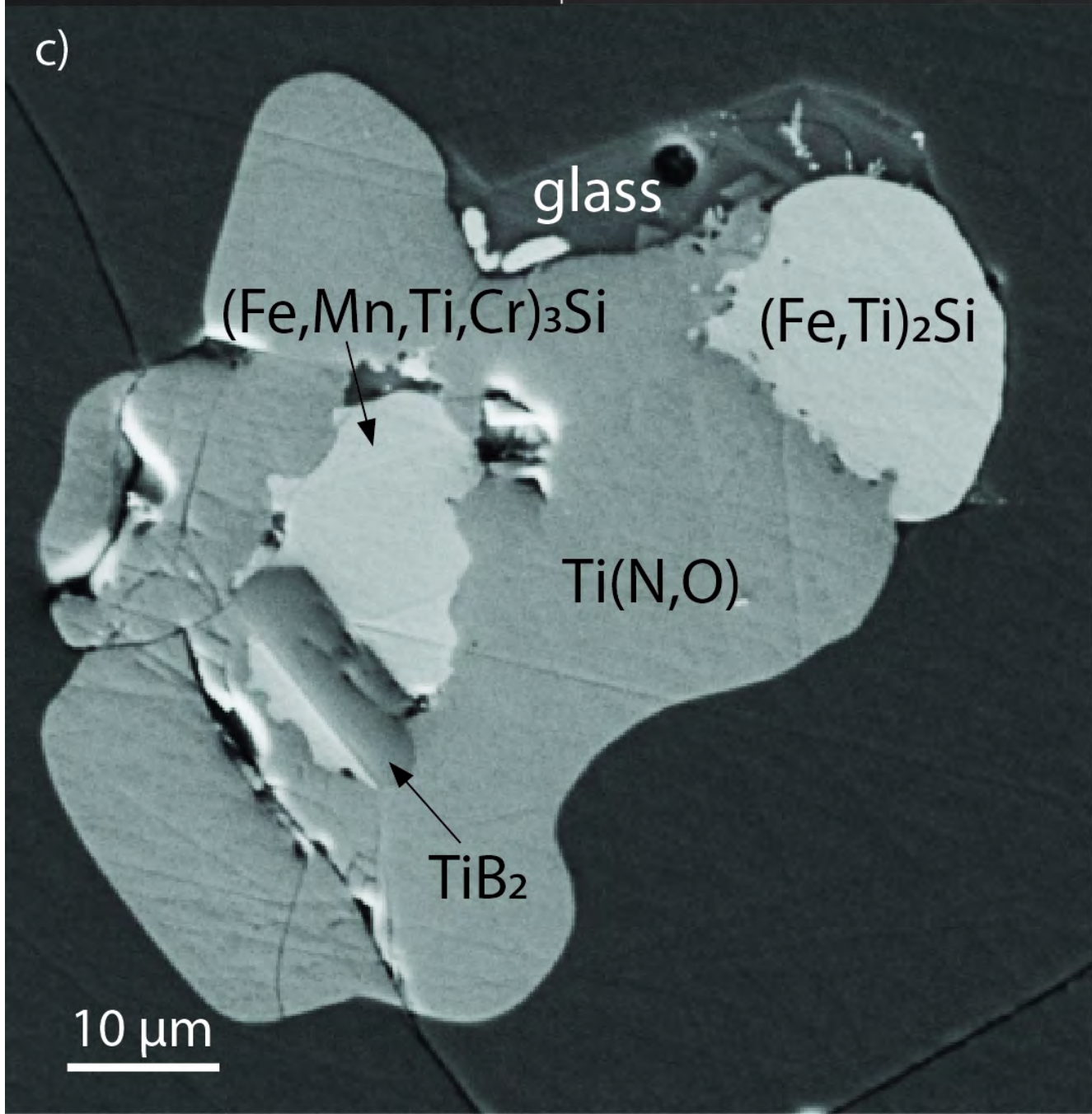
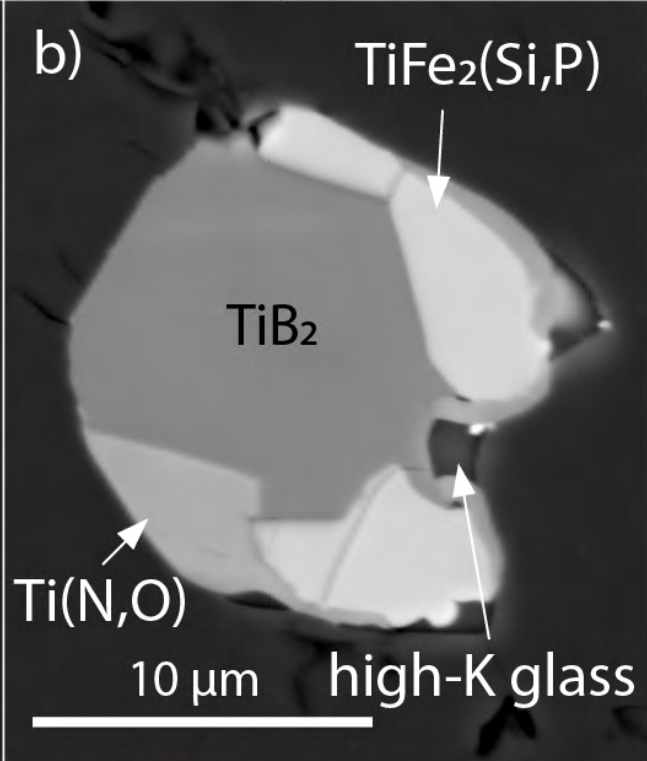
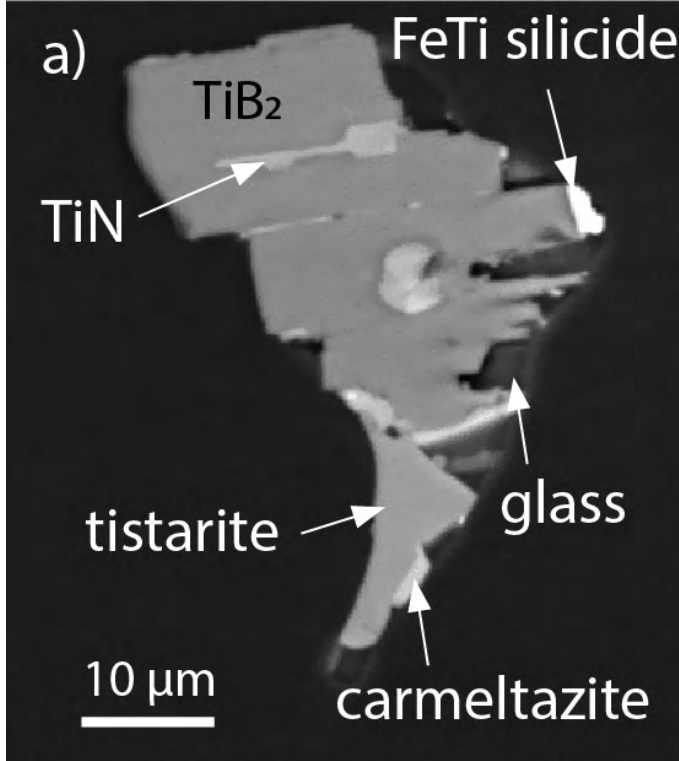
Fe-Ti-Cr silicide

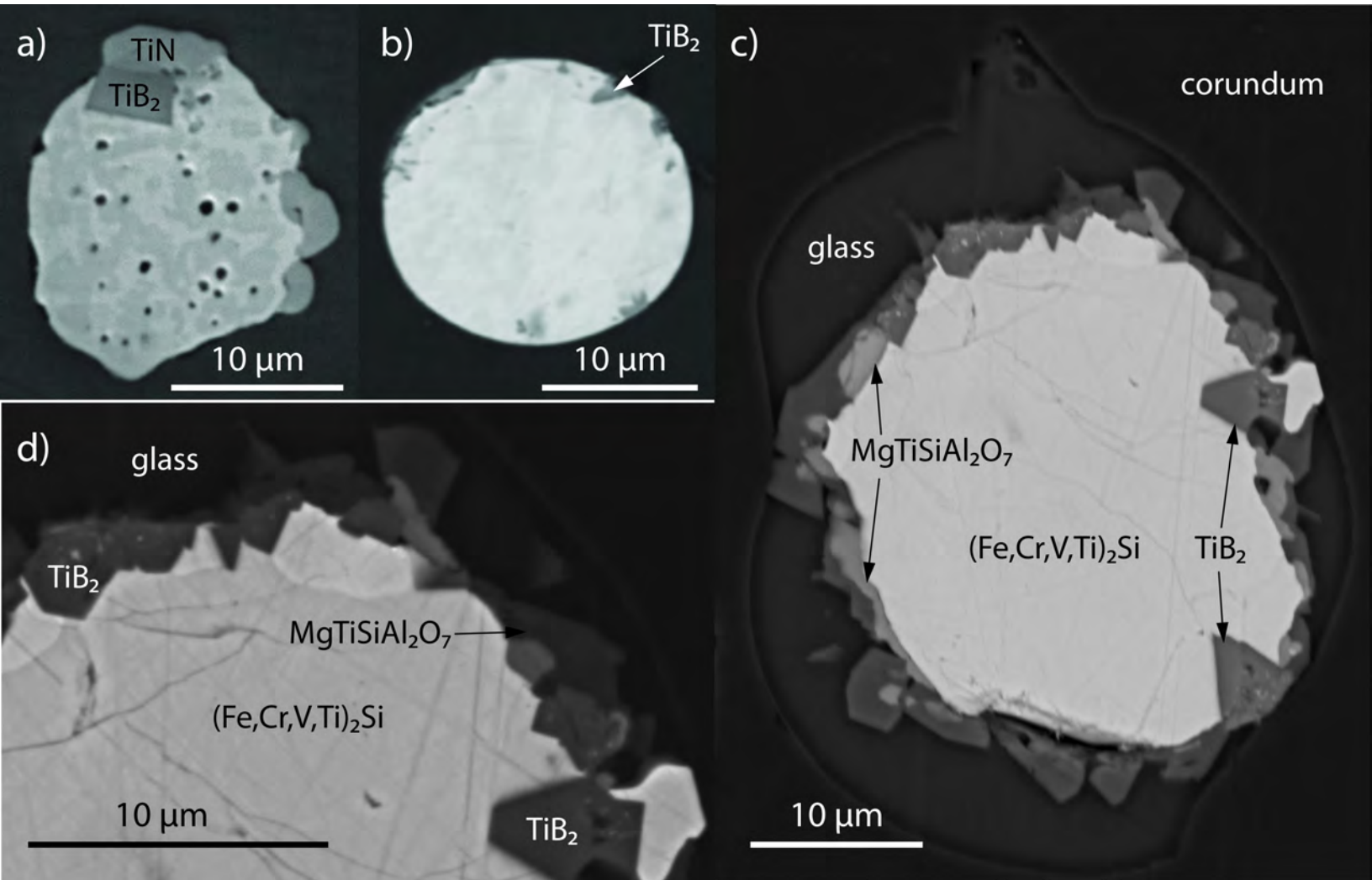
carmeltazite

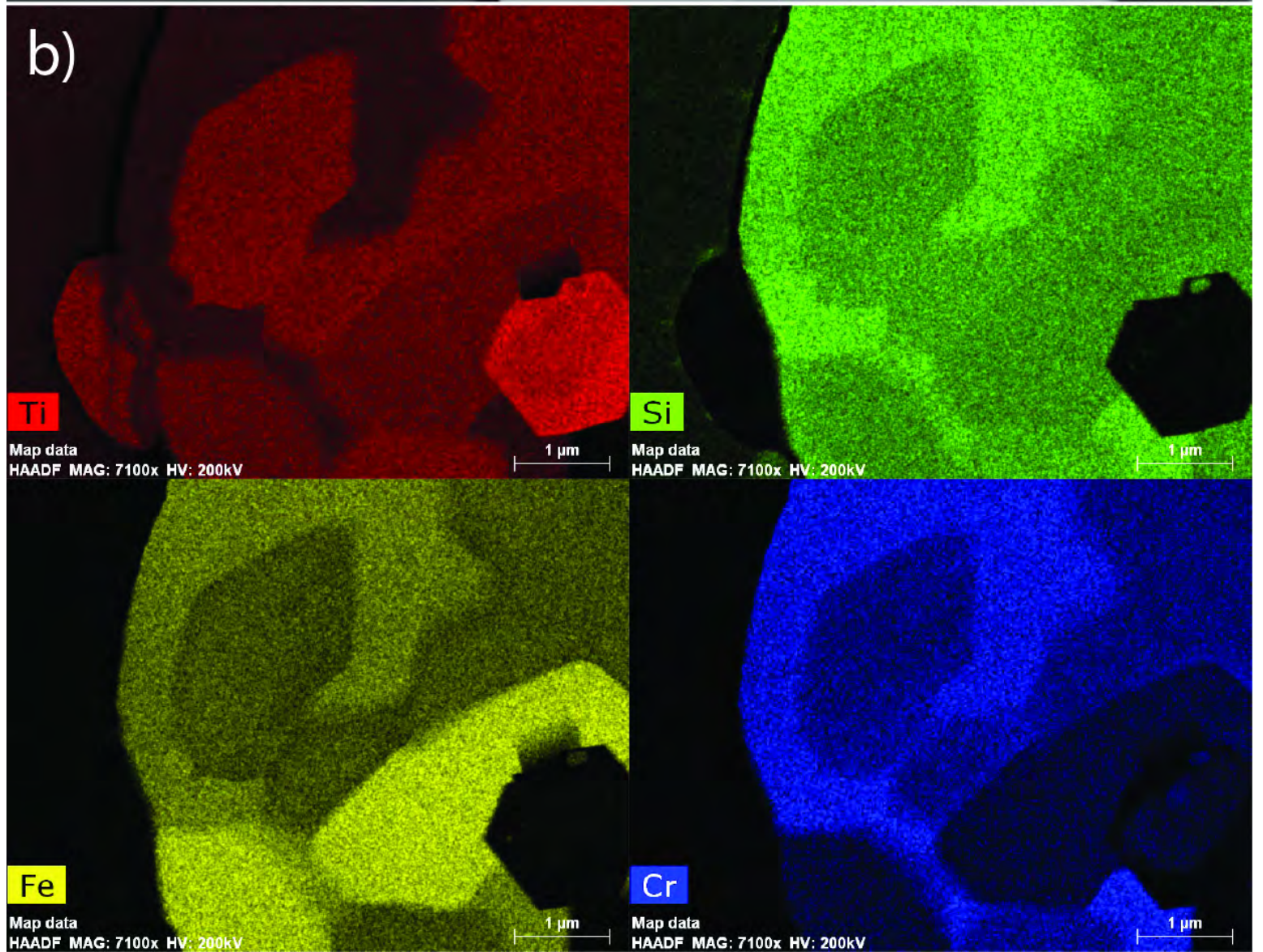
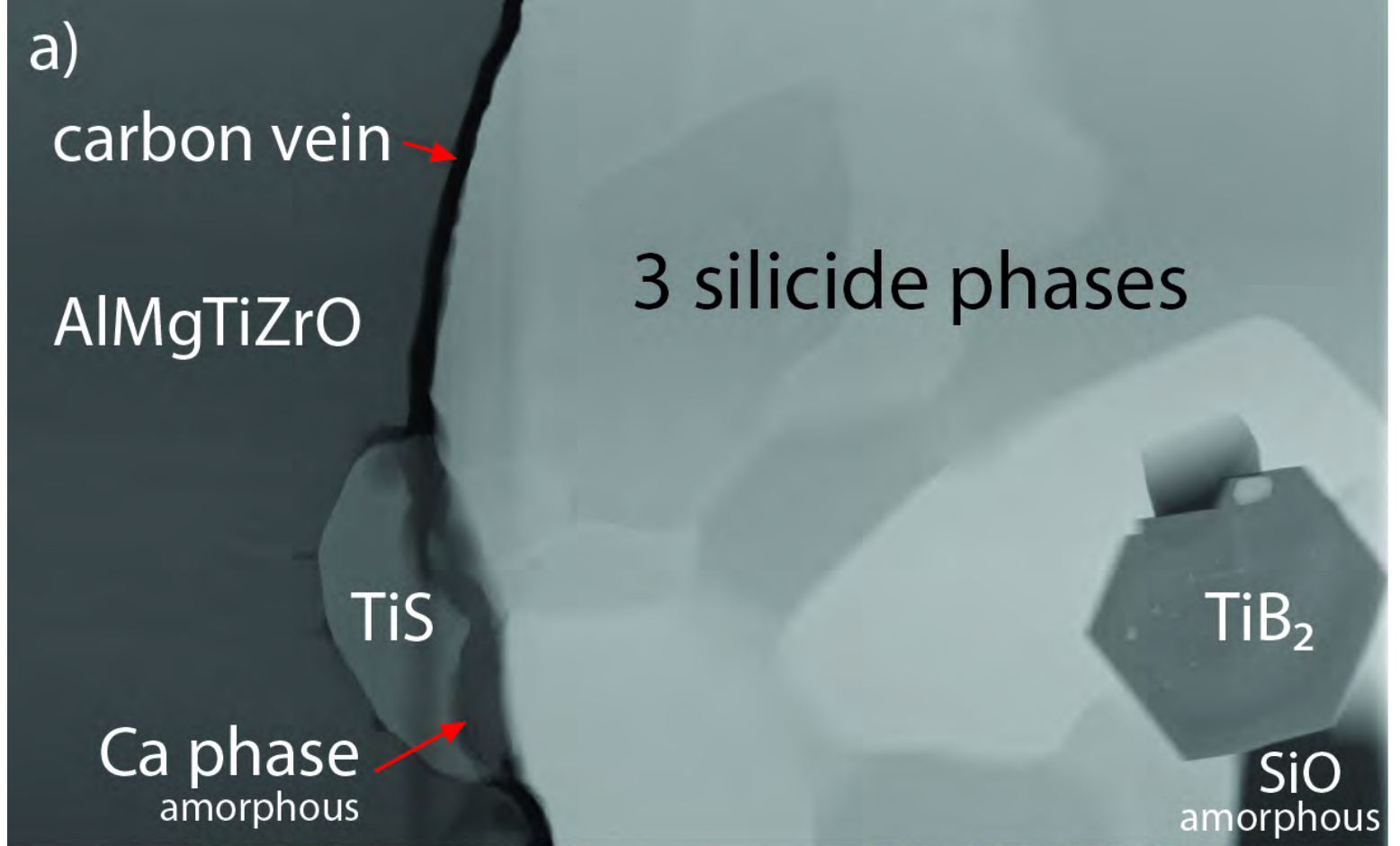
TiAlMgZr oxide

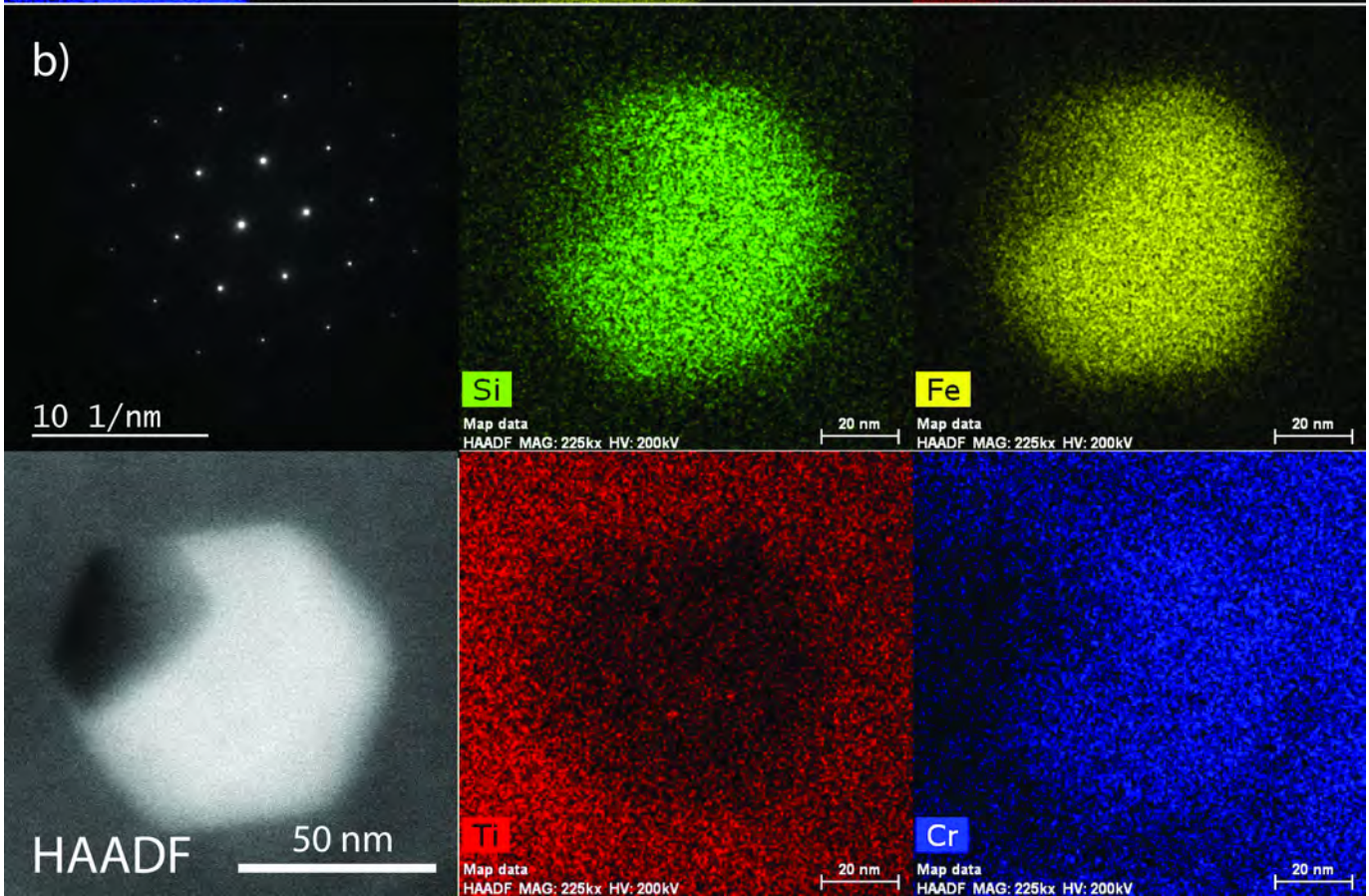
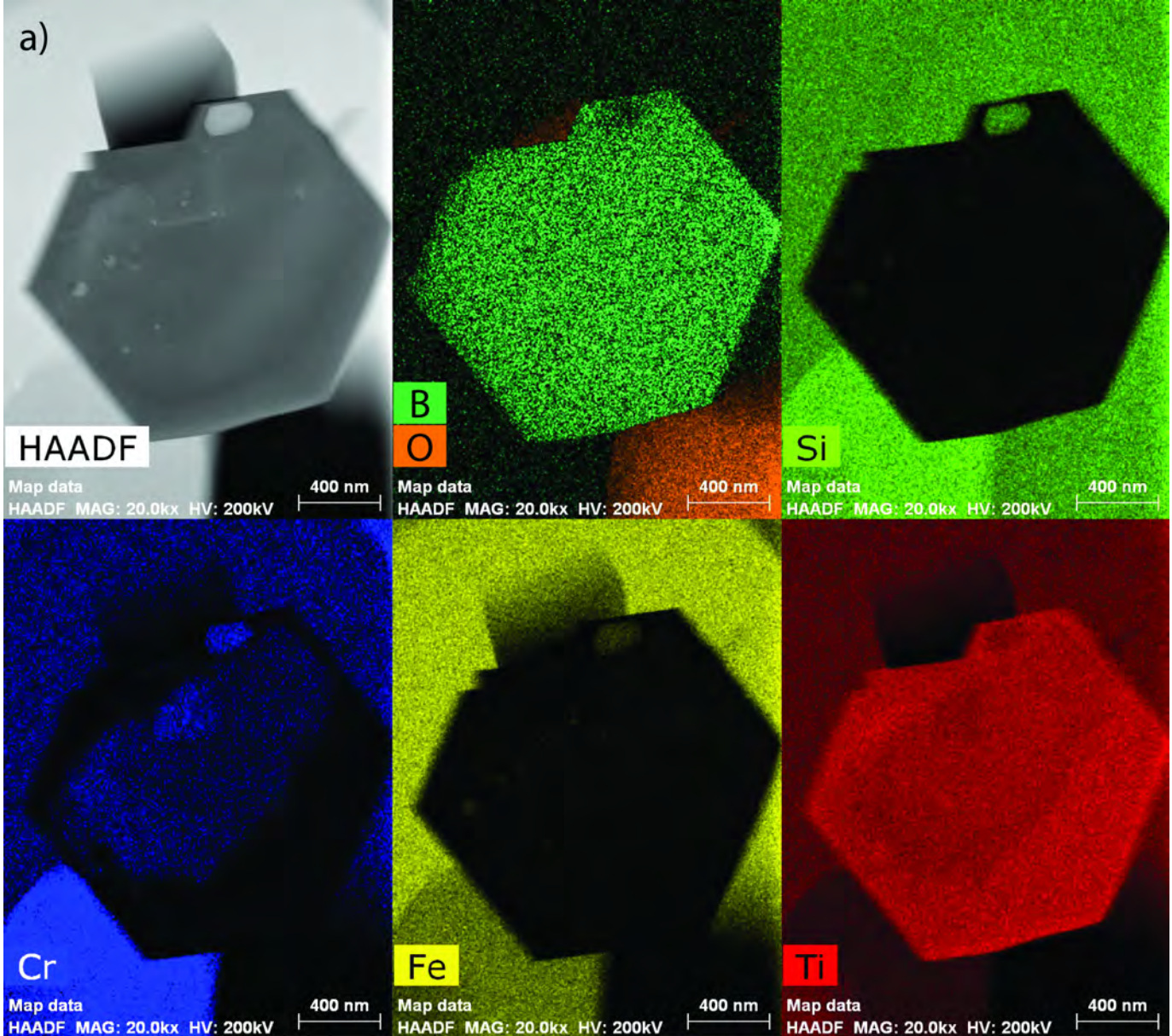
glass

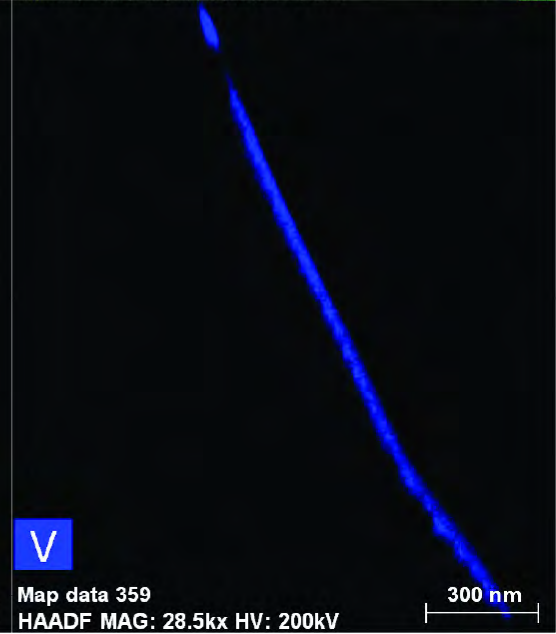
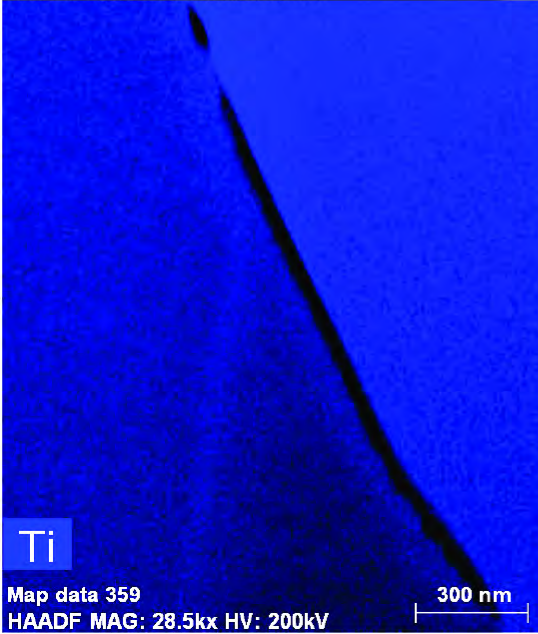
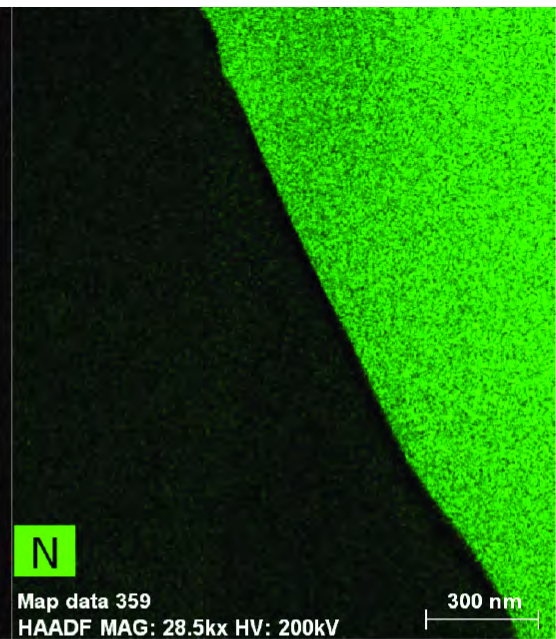
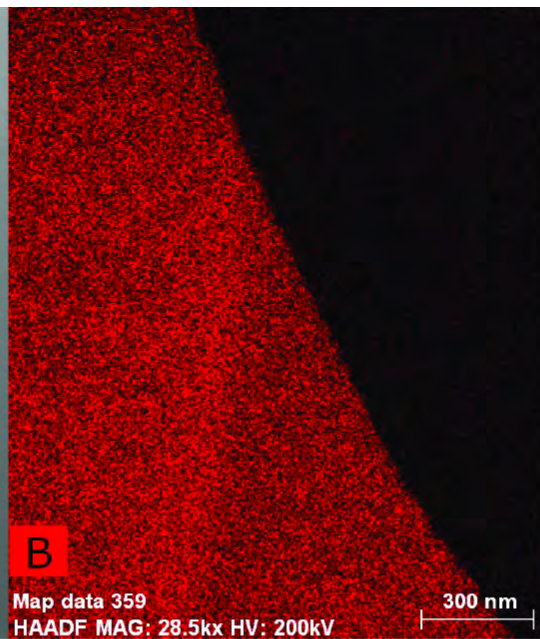
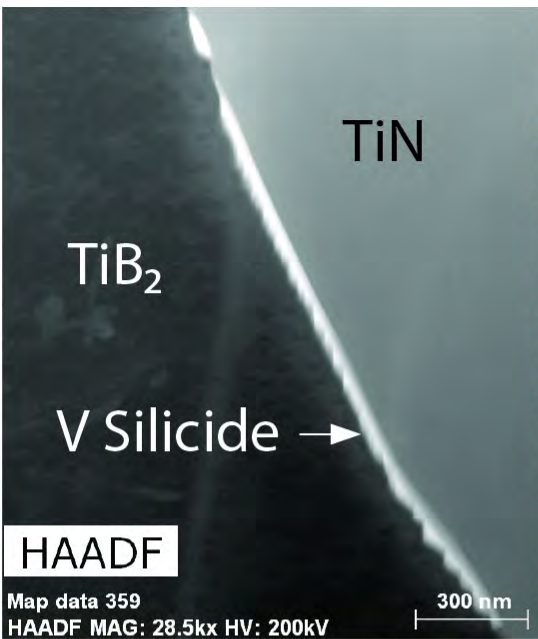
50 μm

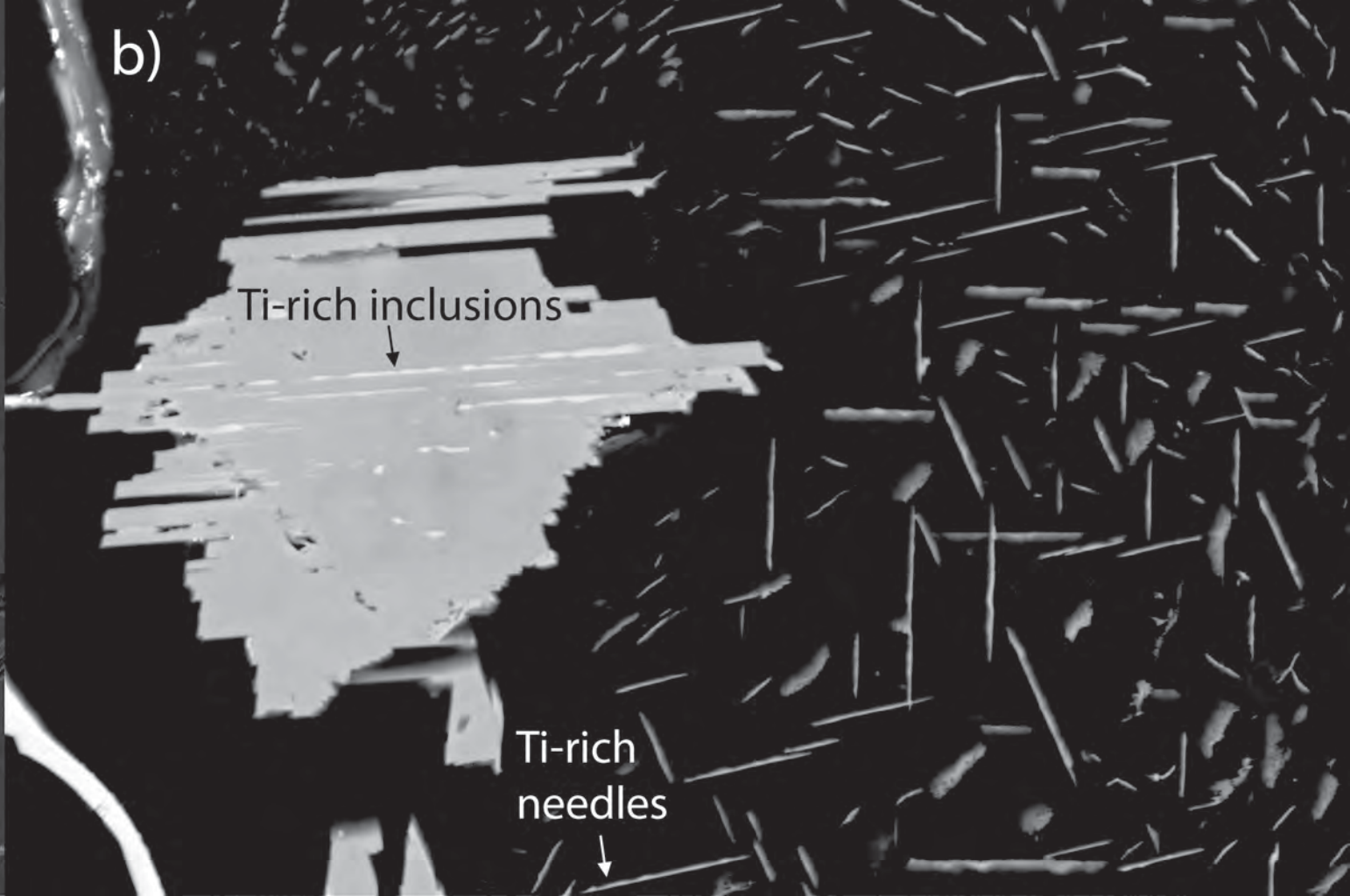
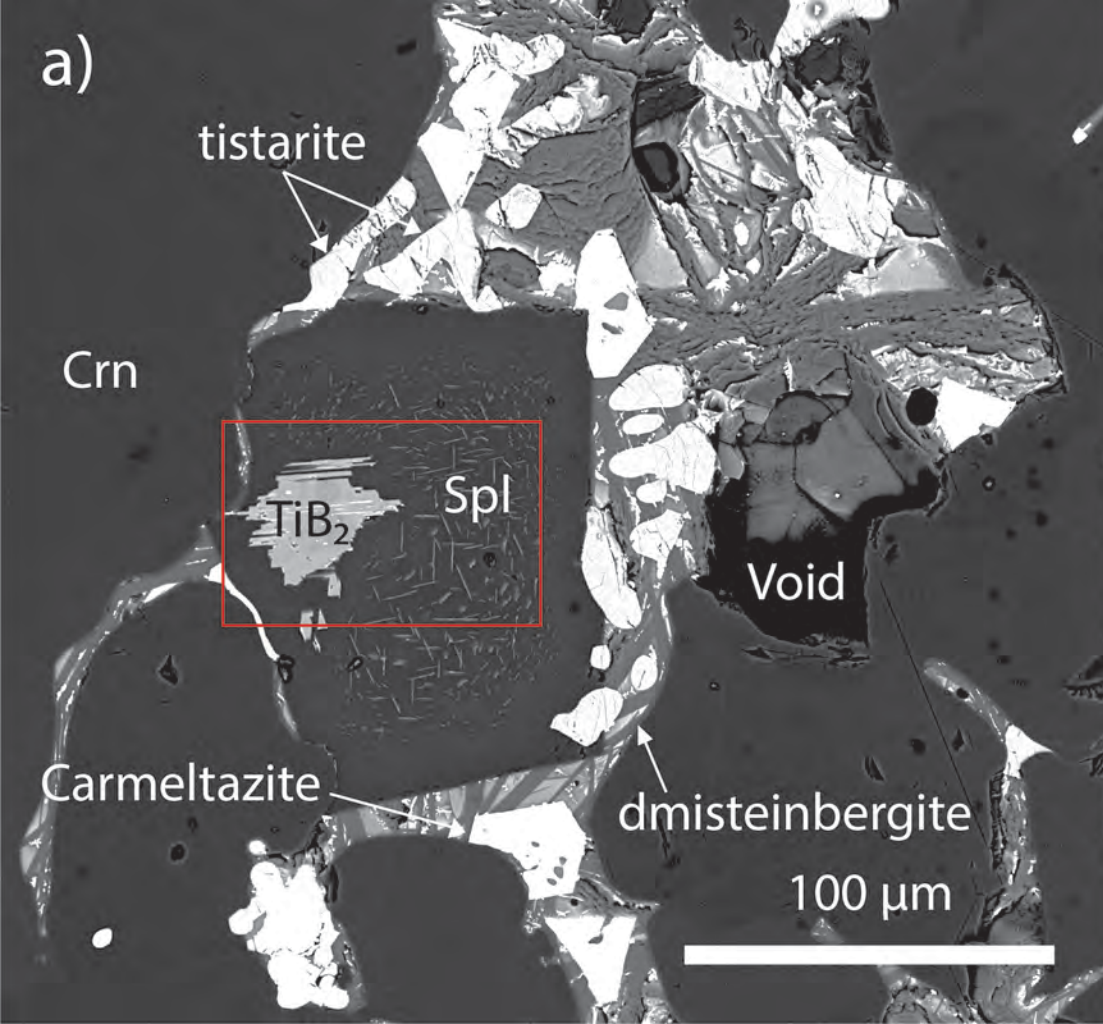


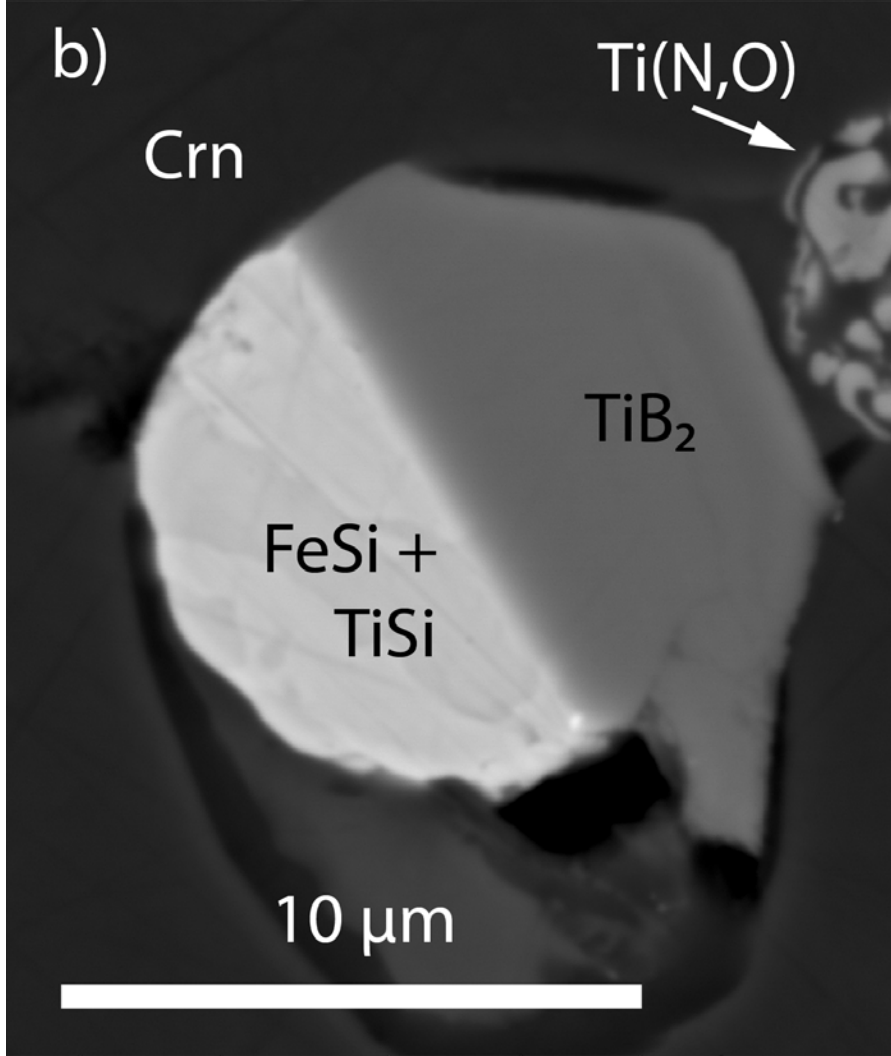
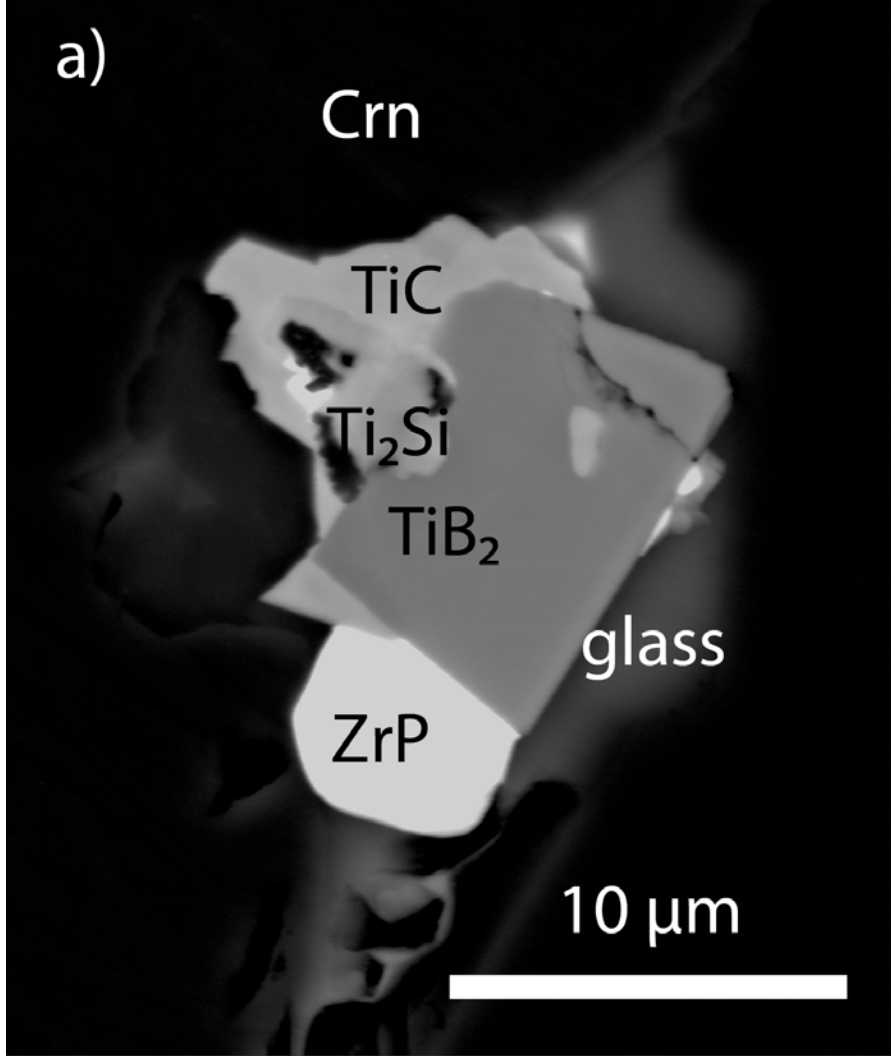


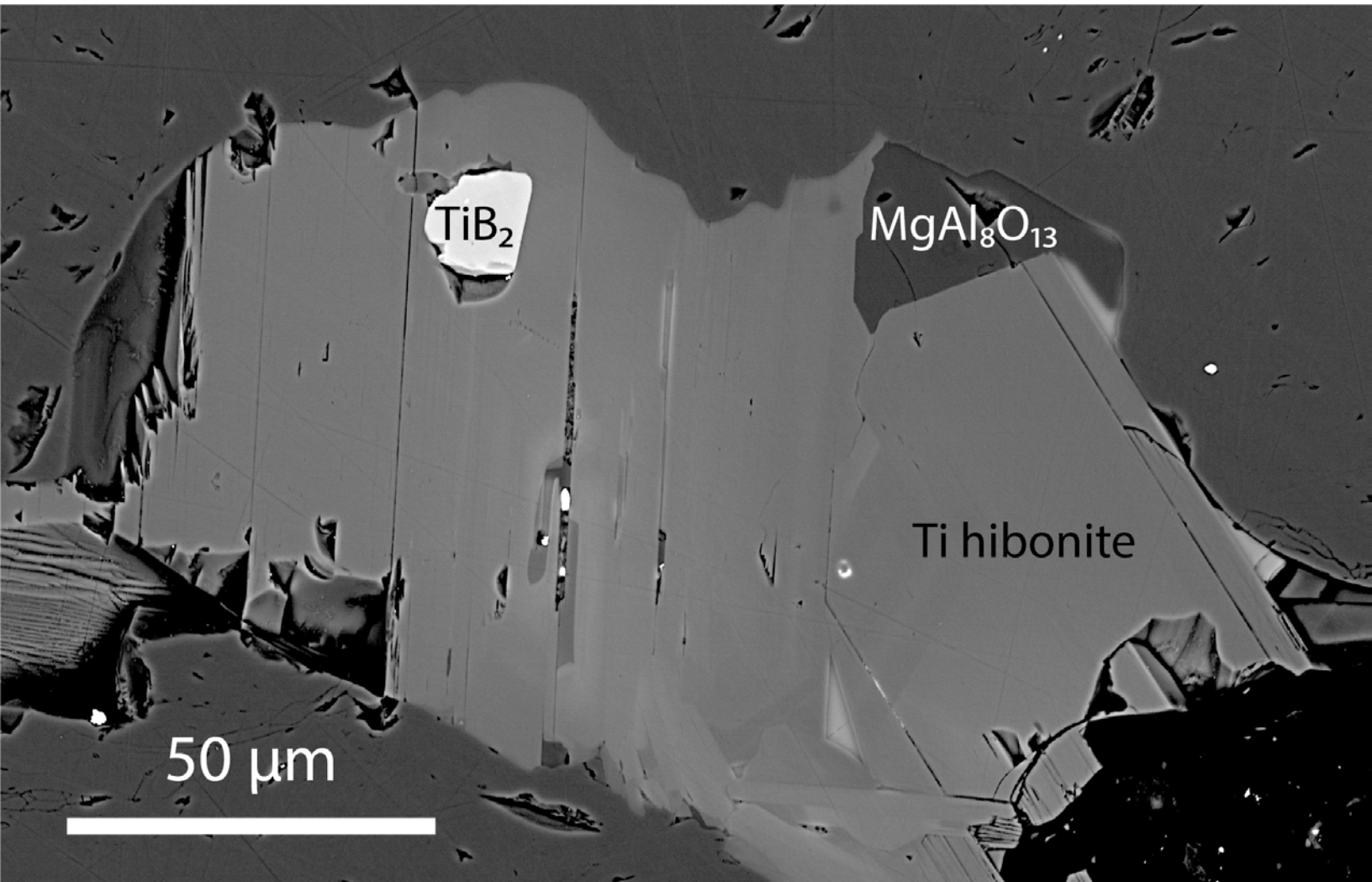












BSE
15kV

Crn

Ti(N,O)

TiB₂

glass

100 μm

